



26 **Abstract**

27

28 CRISPR knockout screens in hundreds of cancer cell lines have revealed a substantial number  
29 of context-specific essential genes that, when associated with a biomarker such as lineage or  
30 oncogenic mutation, offer candidate tumor-specific vulnerabilities for targeted therapies or novel  
31 drug development. Data-driven analysis of knockout fitness screens also yields many other  
32 functionally coherent modules that show emergent essentiality or, in rarer cases, the opposite  
33 phenotype of faster proliferation. We develop a systematic approach to classify these suppressors  
34 of proliferation, which are highly enriched for tumor suppressor genes, and define a network of  
35 145 genes in 22 discrete modules. One surprising module contains several elements of the  
36 glycerolipid biosynthesis pathway and operates exclusively in a subset of AML lines, which we  
37 call Fatty Acid Synthesis/Tumor Suppressor (FASTS) cells. The proliferation suppressor activity  
38 of genes involved in the synthesis of saturated fatty acids, coupled with a more severe fitness  
39 phenotype for the desaturation pathway, suggests that these cells operate at the limit of their  
40 carrying capacity for saturated fatty acids, which we confirmed biochemically. Overexpression of  
41 genes in this module is associated with a survival advantage in an age-matched cohort of AML  
42 patients, suggesting the gene cluster driving an *in vitro* phenotype may be associated with a novel,  
43 clinically relevant subtype.

44

45

46

47 **Introduction**

48

49 Gene knockouts are a fundamental tool for geneticists, and the discovery of CRISPR-based  
50 genome editing<sup>1</sup> and its adaptation to gene knockout screens has revolutionized mammalian  
51 functional genomics and cancer targeting<sup>2-8</sup>. Hundreds of CRISPR/Cas9 knockout screens in  
52 cancer cell lines have revealed background-specific genetic vulnerabilities<sup>9-13</sup>, providing guidance  
53 for tumor-specific therapies and the development of novel targeted agents. Although lineage and  
54 mutation state are powerful predictors of context-dependent gene essentiality, variation in cell  
55 growth medium and environment can also drive differences in cell state, particularly among  
56 metabolic genes<sup>14,15</sup>, and targeted screening can reveal the genetic determinants of metabolic  
57 pathway buffering<sup>16,17</sup>.

58

59 The presence and composition of metabolic and other functional modules in the cell can also be  
60 inferred by integrative analysis of large numbers of screens. Correlated gene knockout fitness  
61 profiles, measured across hundreds of screens, have been used to infer gene function and the  
62 modular architecture of the human cell<sup>18-21</sup>. Data-driven analysis of correlation networks reveals  
63 clusters of functionally related genes whose emergent essentiality in specific cell backgrounds is  
64 often unexplained by the underlying lineage or mutational landscape<sup>21</sup>. Interestingly, in a recent  
65 study of paralogs whose functional buffering renders them systematically invisible to monogenic  
66 CRISPR knockout screens<sup>22,23</sup>, it was shown that the majority of context-dependent essential  
67 genes are constitutively expressed in cell lines<sup>23</sup>. Collectively these observations suggest that  
68 there is much unexplained variation in the genetic architecture, and emergent vulnerability, of  
69 tumor cells.

70

71 Building human functional interaction networks from correlated gene knockout fitness profiles in  
72 cancer cells is analogous to generating functional interaction networks from correlated genetic  
73 interaction profiles in *S. cerevisiae*<sup>24-27</sup>. The fundamental difference between the two approaches  
74 is that, in yeast, a massive screening of pairwise gene knockouts in a single yeast strain was  
75 conducted in order to measure genetic interaction - a dual knockout phenotype more or less  
76 severe than that expected by the combination of the two genes independently. In coessentiality  
77 networks, CRISPR-mediated single gene knockouts are conducted across a panel of cell lines  
78 that sample the diversity of cancer genotypes and lineages. Digenic perturbations in human cells,  
79 a more faithful replication of the yeast approach, are possible with Cas9 and its variants, but

80 library construction, sequencing, and positional biases can be problematic<sup>16,28-34</sup>. Recently, we  
81 showed that an engineered variant of the Cas12a endonuclease, enCas12a<sup>35</sup>, could efficiently  
82 perform multiplex gene knockouts<sup>34</sup>, and we demonstrated its effectiveness in assaying synthetic  
83 lethality between targeted paralogs<sup>23</sup>. These developments in principle enable researchers to  
84 measure how biological networks vary across backgrounds, a powerful approach for deciphering  
85 complex biology<sup>24,36,37</sup>.

86

87 CRISPR perturbations in human cells can result in loss of function alleles that increase as well as  
88 decrease *in vitro* proliferation rates; faster proliferation is an extreme rarity in yeast knockouts.  
89 These fast-growers can complicate predictions of genetic interaction<sup>29</sup> and confound pooled  
90 chemoresistance screens<sup>38</sup>. However, there is no broadly accepted method of identifying these  
91 genes from CRISPR screens. Here we describe the development of a method to systematically  
92 classify genes whose knockout provides a proliferation advantage *in vitro*. We observe that genes  
93 which confer proliferation advantage are typically tumor suppressor genes, and that they show  
94 the same modularity and functional coherence as context-dependent essential genes. Moreover,  
95 we discover a novel module that includes several components of the glycerolipid biosynthesis  
96 pathway that slows cell proliferation in a subset of acute myeloid leukemia (AML) cell lines. We  
97 show a rewired genetic interaction network using enCas12a multiplex screening, and find strong  
98 genetic interactions corroborated by clinical survival data. A putative tumor-suppressive role for  
99 glycerolipid biosynthesis is surprising and disconcerting, since this process is thought to be  
100 required to generate biomass for tumor cell growth, and inhibitors targeting this pathway are  
101 currently in clinical trials<sup>39,40</sup>.

102

## 103 **Results**

104

### 105 ***Identifying Proliferation Suppressor Signatures***

106

107 We previously observed genes whose knockout leads to overrepresentation in pooled library  
108 knockout screens. These genes, which we term proliferation suppressor genes (PSG), exhibit  
109 positive selection in fitness screens, a phenotype opposite that of essential genes. As expected,  
110 many PSG are known tumor suppressor genes; for example, *TP53* and related pathway genes  
111 *CDKN1A*, *CHEK2*, and *TP53BP1* show positive selection in select cell lines (**Figure 1a**).  
112 Detection of these genes as outliers is robust to the choice of CRISPR analytical method, as we  
113 tested BAGEL2<sup>41,42</sup>, CERES<sup>10</sup>, JACKS<sup>43</sup>, and mean log fold change (LFC) of gRNA targeting each

114 gene (**Supplementary Figure 1a-d**). Unlike core-essential genes, PSG are highly context-  
115 specific: *TP53* knockout shows positive LFC only in cell lines with wild-type *TP53* (**Figure 1b**),  
116 and *PTEN* knockout shows the PS phenotype only in *PTEN*<sup>wt</sup> backgrounds (**Figure 1c**). These  
117 observations are consistent with the knockout phenotypes of known tumor suppressor genes  
118 (TSG) in cell lines: in wildtype cells, TSG knockout increases the proliferation rate in cell culture,  
119 but when cell lines are derived from tumors where the TSG is already lost or non-functional, gene  
120 knockout has no effect. TSG are therefore context-specific PSG, but it is not necessarily the case  
121 that genes with a proliferation suppressor phenotype *in vitro* act as TSG *in vivo*; proliferation  
122 suppressors are at best putative tumor suppressors in the absence of confirmatory data from  
123 tumor profiling.

124  
125 Though detection of PSG is possible using existing informatics pipelines, several factors  
126 complicate a robust detection of these genes. There is no accepted threshold for any algorithm  
127 we considered to detect PSG, since all were optimized to classify essential genes. A related  
128 second issue is that cell line screens show a wide range of variance in LFC distributions, making  
129 robust outlier detection challenging (**Supplementary Figure 1e-f**). Third, the signatures are  
130 strongly background-dependent, as demonstrated by *PTEN* and *TP53*. Finally, there is no  
131 consistent expectation for whether or how many putative tumor suppressor genes are present in  
132 a given cell line.

133  
134 To address this gap, we developed a method to account for variability in fold-change distributions  
135 between screens. Our approach uses a Gaussian mixture model (K=2) to estimate each screen's  
136 distribution of gene-level LFC scores (**Figure 1a**). Mixed distribution models have previously been  
137 used to identify distinctions between populations of essential and nonessential fitness genes in  
138 CRISPR screens<sup>44</sup>. For the  $K = 2$  mixture model, the more negative distribution (**Figure 1a**, red)  
139 is generally essential genes, while the higher, narrower peak around zero (**Figure 1a**, blue),  
140 models the large population of knockouts with no fitness phenotype. We used this second model  
141 to calculate a Z-score (hereafter referred to as the 'mixed Z-score') for all gene-level mean fold  
142 changes in each cell line. This approach normalizes variance (**Supplementary Figure 1e-f**)  
143 across LFC distributions in different cell lines, with negative Z-scores indicating essential genes  
144 and positive Z-scores representing PSG phenotypes.

145  
146 To evaluate the effectiveness of this mixed Z-score approach, we used COSMIC<sup>45,46</sup> tumor  
147 suppressor genes as a true positive reference set, and we combined COSMIC-defined oncogenes

148 (removing dual-annotated tumor suppressors) with our previously-specified set of nonessential  
149 genes as a true negative reference set<sup>7,47</sup>. Since there is no expectation for the presence of a  
150 consistent set of PSG across cell lines, we analyzed each of the 808 cell lines from the Avana  
151 2020Q4 data release independently<sup>10,48,49</sup> calculating gene-level scores on each cell line  
152 individually and then combining all scores into a master list of  $808 \times 18k = 14.6$  million gene-cell  
153 line observations (**Supplementary Table 1**). Moreover, since there is also no expectation that all  
154 COSMIC TSG would be detected cumulatively across all cell lines, we judged that traditional recall  
155 metrics (e.g. percentage of the reference set recovered) were inappropriate. We therefore defined  
156 recall as the total number of TSG-cell line observations. Using this evaluation scheme, the mixed  
157 Z-score approach outperforms comparable methods by a substantial margin, classifying more  
158 than 722 PS-cell line instances at a 10% false discovery rate (FDR) (**Figure 1d**). This is roughly  
159 50% more putative PSG than the closest alternative, a nonparametric rank-based approach, at  
160 the same FDR. BAGEL<sup>41,42</sup>, a supervised classifier of essential genes, performed worst at TSG,  
161 and the raw mean LFC approach also fared poorly, highlighting the need for variance  
162 normalization across experiments. We applied this 10% FDR threshold for all subsequent  
163 analyses.

164

165 Common tumor suppressor genes PTEN and TP53 were observed in ~15% of cell lines (**Figure**  
166 **1e**), with other well-known TSG appearing less frequently. Among 309 COSMIC TSGs for which  
167 we have fitness profiles (representing 1.7% of all 18k genes), we find that 116 (37.5%) of these  
168 genes occur as proliferation suppressors at least once (**Supplementary Table 2**) and make up  
169 24.4% of total proliferation suppressor calls (**Supplementary Figure 2a-b**), a 14-fold enrichment.  
170 All of the known TSG hits come from just 504 of the 808 cell lines (62.4%) in which proliferation  
171 suppressor hit calls were identified (**Figure 1f**), yet we did not observe a bias toward particular  
172 tissues: in every lineage, most cell lines carried at least one PSG (**Supplementary Figure 1g**).  
173

174 To further validate our approach, we compared the set of TSGs in our PSG hits to other molecular  
175 profiling data. When identified as a proliferation suppressor, 53% of the 116 TSGs demonstrate  
176 higher mean mRNA expression relative to backgrounds where the same TSG is not a proliferation  
177 suppressor (**Supplementary Table 2**). Similarly, 96.6% of the 116 TSGs, when classified as a  
178 proliferation suppressor, demonstrate lower frequency of nonsilent mutations compared to  
179 backgrounds where the TSG is not a hit (**Supplementary Table 2**). These observations were not  
180 restricted to COSMIC TSGs however, as this was the case for all PSG hit calls of genes against  
181 non-PSG hit calls (**Supplementary Figure 2c and 2d**). Copy number comparisons did not

182 suggest major distinctions between PSG vs non-PSG calls (**Supplementary Figure 2e**), however  
183 there did appear to be more variation in PSG observations, possibly stemming from smaller  
184 grouped sample sizes. Together, these observations confirm the reliability of our method to detect  
185 genes whose knockout results in faster cell proliferation, and that, analogous to essential genes,  
186 these genes must be expressed and must not harbor a loss-of-function mutation in order to elicit  
187 this phenotype.

188

189 We attempted to corroborate our findings using a second CRISPR dataset of 342 cell line screens  
190 from Behan *et al.*<sup>13</sup>, including >150 screens in the same cell lines as in the Avana data. However,  
191 these screens were conducted over a shorter timeframe than the Avana screens (14 vs. 21 days),  
192 giving less time for both positive and negative selection signals to appear (see Methods for a  
193 detailed discussion). As a result, when we compared cell lines screened by both groups, the  
194 Avana data yielded many more TSG hits (**Supplementary Figure 3a**). While most of these do  
195 not meet our threshold for PSG in the Sanger data, hits at our 10% FDR threshold across all  
196 Avana screens are strongly biased toward positive mixed Z-scores in the Sanger screens  
197 (**Supplementary Figure 3b**), consistent with a weaker signal of positive selection as a result of  
198 the shorter assays rather than a lack of robustness in the screens<sup>49</sup>.

199

200 ***Discovering Pathways Modulating Cell Growth with a Proliferation Suppressor Co-  
201 Occurrence Network***

202

203 Although known TSG act as PSG in only a subset of cell lines, we observed patterns of co-  
204 occurrence among functionally related genes. *PTEN* co-occurs with mTOR regulators *NF2*<sup>50</sup> ( $P <$   
205  $3 \times 10^{-11}$ , Fisher's exact test) and the *TSC1/TSC2* complex ( $P$ -values both  $< 7 \times 10^{-13}$ )<sup>51</sup>, as well as  
206 Programmed Cell Death 10 (*PDCD10*)<sup>52</sup>, a proposed tumor suppressor<sup>7,53</sup> (**Figure 2a**). The p53  
207 regulatory cluster (*TP53*, *CDKN1A*, *CHECK2*, *TP53BP1*) also exhibited a strong co-occurrence  
208 pattern that was independent of the mTOR regulatory cluster (**Figure 2a**). mTOR<sup>54</sup> and cell cycle  
209 checkpoint genes<sup>55,56</sup> have been heavily linked to cancer development, given their roles in  
210 controlling cell growth and proliferation, and thus have been the focus of studies characterizing  
211 patient genomic profiles to identify common pathway alterations<sup>57,58</sup>.

212

213 The modularity of mTOR regulators and TP53 regulators demonstrates pathway-level  
214 proliferation suppressor activity. This reflects the concept of genes with correlated fitness profiles  
215 indicating the genes operate in the same biochemical pathway or biological process<sup>19,21,59,60</sup>.

216 However, the sparseness of PSG, coupled with their smaller effect sizes, renders correlation  
217 networks relatively poor at identifying modules of genes with proliferation suppressor activity. In  
218 order to identify such modules, we developed a PSG network (**Supplementary Table 3**) based  
219 on statistical overrepresentation of co-occurring PSG (**Figure 2b**); see Methods for details. This  
220 approach yields a network of 145 genes containing 462 edges in disconnected clusters; only 8  
221 clusters have 3 or more genes (**Figure 2c** and **Supplementary Figure 4c**). Of these 462 edges,  
222 74 (16.0%, empirical  $P < 10^{-4}$ ) are present in the HumanNet<sup>61</sup> functional interaction network  
223 (**Supplementary Figure 4a-b**), ~8 fold more than expected from random sampling, indicating high  
224 functional coherence between connected genes. The network recovers the PTEN and TP53  
225 modules as well as the Hippo pathway, the aryl hydrocarbon receptor complex (AHR/ARNT), the  
226 mTOR-repressing GATOR1 complex, the STAGA chromatin remodeling complex, JAK-STAT  
227 signaling, and the gamma-secretase complex (**Figure 2c, and Supplementary 4c**), all of which  
228 have been associated with tumor suppressor activity. The functional coherence and biological  
229 relevance of the PSG co-occurrence network further validates the approach taken and establishes  
230 this dataset as a resource for exploring putative tumor suppressor activity in cell lines and tumors.  
231

### 232 **Variation in Fatty Acid Metabolism in AML Cells**

233  
234 In addition to the known tumor suppressors, we observed a large module containing elements of  
235 several fatty acid (FA) and lipid biosynthesis pathways (**Figure 2c**). Interestingly, while there does  
236 not appear to be a strong tissue specificity signature for most clusters (**Figure 2c**), the fatty acid  
237 metabolism cluster shows a strong enrichment for AML cell lines ( $P = 1.5 \times 10^{-4}$ ). AML, like most  
238 cancers, typically relies on increased glucose consumption for energy and diversion of glycolytic  
239 intermediates for the generation of biomass required for cell proliferation. Membrane biomass is  
240 generated by phospholipid biosynthesis that uses fatty acids as building blocks, with FA pools  
241 replenished by some combination of triglyceride catabolism, transporter-mediated uptake, and *de*  
242 *novo* synthesis via the *ACLY/ACACA/FASN* palmitate production pathway using citrate precursor  
243 diverted from the TCA cycle. Indeed, the role of lipid metabolism in AML progression is indicated  
244 by changes in serum lipid content<sup>62</sup>, in particular for long-chain saturated fatty acids that are the  
245 terminal product of the FAS pipeline. Inhibition of FA synthesis is therefore an appealing  
246 chemotherapeutic intervention<sup>63,64</sup> and FASN inhibitors are currently undergoing clinical trials for  
247 treatment of solid tumors and metabolic diseases<sup>40</sup>. The observation that knocking out FAS  
248 pathway genes results in *faster* proliferation in some AML cells, and their signature as putative  
249 tumor suppressor genes, is therefore very unexpected.

250

251 To learn whether additional elements of lipid metabolism were associated with the FAS cluster,  
252 we examined the differential correlation of mixed Z-scores in AML cells. We and others have  
253 shown that genes with correlated gene knockout fitness profiles in CRISPR screens are likely to  
254 be involved in the same biological pathway or process ("co-functional")<sup>18-21</sup>, analogous to  
255 correlated genetic interaction profiles in yeast<sup>25,26,65</sup>. Strikingly, all gene pairs within the fully  
256 connected clique in the FAS cluster (containing genes *FASN*, *ACACA*, *GPAT4*, *CHP1*, *GPI*  
257 *CERS6*, *PCGF1*, **Figure 2c**) had a median Pearson correlation coefficient (PCC) of 0.76 in the  
258 23 AML cell lines (range 0.63-0.95, **Figure 3a**, red), compared to median correlation of 0.05 in  
259 the remaining 785 cell lines (range -0.11-0.62, with the highest correlation between *FASN* and  
260 *ACACA*, adjacent enzymes in the linear palmitate synthesis pathway; **Figure 3a**, gray). These  
261 high differential Pearson correlation coefficients (dPCC) suggest that variation in lipid metabolism  
262 is pronounced in AML cells<sup>66</sup>.

263

264 We sought to explore whether this difference in correlation identified other genes that might give  
265 insight into metabolic rewiring in AML. We first removed noisy data by filtering for high-quality  
266 screens (Cohen's D > 2.5, recall > 60%<sup>42</sup>), leaving 659 cell lines, including 17 AML cell lines.  
267 Calculating a global difference between PCC of all gene pairs in all 17 AML and in the remaining  
268 642 cell lines yielded many gene pairs whose dPCC appeared indistinguishable from random  
269 sampling (**Supplementary Figure 5a-b**). To filter these, we calculated empirical P-values for  
270 each gene pair. We randomly selected 17 cell lines from the pool of all screens, calculated PCC  
271 for all gene pairs in the selected and remaining lines, and calculated dPCC from these PCC values  
272 (**Figure 3b**). We repeated this process 1,000 times to generate a null distribution of dPCC values  
273 for each gene pair, against which a P-value could be computed (**Figure 3c-d**).

274

275 Expanding the set to a filtered list of genes whose correlation with a gene in the FAS clique  
276 showed significant change in AML cells (P<0.001; see Methods) yielded a total of 106 genes,  
277 including the 7 genes in the clique (**Figure 3e**) plus Holocarboxylase Synthetase (*HLCS*), which  
278 biotinylates and activates acetyl-CoA-carboxylase, the protein product of *ACACA*, as well as  
279 glycolysis pathway genes *PGP* and *HK2*. Interestingly, about half of the genes showed  
280 significantly increased anticorrelation with the FAS cluster, indicating genes preferentially  
281 essential where the FAS genes act as proliferation suppressors (**Figure 3e**). These genes include  
282 fatty acid desaturase (*SCD*), which operates directly downstream from *FASN/ACACA* to generate

283 monounsaturated fatty acid species, and Sterol Regulatory Element Binding Transcription Factor  
284 1 (*SREBF1*), the master regulatory factor for lipid homeostasis in cells.

285  
286 Clustering the AML cell lines according to these high-dPCC genes reveals two distinct subsets  
287 of cells. The FAS cluster and its correlates show strong proliferation suppressor phenotype in four  
288 cell lines, NB4, MV411, MOLM13, and THP1. The remaining thirteen AML cell lines show  
289 negligible to weakly essential phenotypes when these genes are knocked out. The anticorrelated  
290 genes, including *SCD* and *SREBF1*, show heightened essentiality in these same cell lines.  
291 Together these observed shifts in gene knockout fitness indicates that this subset of AML cells  
292 has a substantial metabolic rewiring. Because these cells share a genetic signature among fatty  
293 acid synthesis pathway genes that is consistent with tumor suppressors, we call these cell lines  
294 Fatty Acid Synthesis/Tumor Suppressor (FASTS) cells (**Figure 3e**).  
295

#### 296 ***Cas12a-mediated Genetic Interaction Screens Confirm Rewired Lipid Metabolism***

297  
298 We sought to confirm whether gene knockout confers improved cell fitness, and to gather some  
299 insight into why some AML cells show the FASTS phenotype and others do not. Genetic  
300 interactions have provided a powerful platform for understanding cellular rewiring in model  
301 organisms, and we sought to apply this approach to deciphering the FASTS phenotype. We  
302 designed a CRISPR screen that measures the genetic interactions between eight selected “query  
303 genes” and ~100 other genes (“array genes”). The query genes include *FASN* and *ACACA*, from  
304 the cluster of proliferation-suppressor genes, as well as lipid homeostasis transcription factor  
305 *SREBF1*, anticorrelated with the FAS cluster in the differential network analysis, and  
306 uncharacterized gene *c12orf49*, previously implicated in lipid metabolism by coessentiality<sup>21</sup> and  
307 a recent genetic interaction study<sup>60</sup>. Additional query genes include control tumor suppressor  
308 genes *TP53* and *PTEN* and control context-dependent essential genes *GPX4* and *PSTK* (**Figure**  
309 **4a**). The array genes include two to three genes each from several metabolic pathways, including  
310 various branches of lipid biosynthesis, glycolysis and glutaminolysis, ophox, peroxisomal and  
311 mitochondrial fatty acid oxidation. We include the query genes in the array gene set (**Figure 4a**)  
312 to test for screen artifacts and further add control essential and nonessential genes to measure  
313 overall screen efficacy (**Supplementary Table 4-5**).  
314

315 We used the enCas12a CRISPR endonuclease system to carry out multiplex gene knockouts<sup>35</sup>.  
316 We used a dual-guide enCas12a design, as described in DeWeirdt *et al.*<sup>34</sup>, that allows for

317 construction of specific guide pairs through pooled oligonucleotide synthesis (**Figure 4b**). The  
318 library robustly measures single knockout fitness by pairing three Cas12a crRNA per target gene  
319 each with five crRNA targeting nonessential genes<sup>7,47</sup> (n=15 constructs for single knockout  
320 fitness), and efficiently assays double knockout fitness by measuring all guides targeting query-  
321 array gene pairs (n=9) (**Figure 4c & Supplementary Table 5**). Using this efficient design and the  
322 endogenous multiplexing capability of enCas12a, we were able to synthesize a library targeting  
323 800 gene pairs with a single 12k oligonucleotide array.

324

325 We screened one AML cell line from the FASTS subset, MOLM13, and a second one with no FAS  
326 phenotype, NOMO1, collecting samples at 14 and 21 days after transduction with a five-day  
327 puromycin selection (**Supplementary Table 6-7**). Importantly, by comparing the mean log fold  
328 change of query gene knockouts in the “A” position vs. the same genes in the “B” position of the  
329 dual knockout vector, we find no positional bias in the multiplex knockout constructs (**Figure 4d**),  
330 consistent with our previous findings<sup>23,34</sup>. Single knockout fitness measurements effectively  
331 segregated known essential genes from nonessentials, confirming the efficacy of the primary  
332 screens (**Supplementary Figure 6**). Context-dependent fitness profiles are consistent with the  
333 cell genotypes, with *PTEN* and *TSC1* showing positive selection in *PTEN*<sup>wt</sup> NOMO1 cells and  
334 *TP53* being a strong PS gene in *P53*<sup>wt</sup> MOLM13 cells. Strikingly, *CHP1* and *GPAT4* are the next  
335 two top hits in MOLM13, confirming their proliferation suppressor phenotype (**Figure 4e**), while  
336 neither shows a phenotype in NOMO1. Together these observations validate the enCas12a-  
337 mediated multiplex perturbation platform, confirm the ability of CRISPR knockout screens to  
338 detect proliferation suppressors, and corroborate the background-specific fitness enhancing  
339 effects of genes from the FAS cluster.

340

341 To measure genetic interactions, we fit a linear regression for each guide between the  
342 combination LFCs and the single guide LFCs, Z-scoring the residuals from this line, and  
343 combining across all guides targeting the same gene pair (**Supplementary Figure 6 &**  
344 **Supplementary Table 7**). Here, positive genetic interaction Z-scores reflect greater fitness than  
345 expected and negative Z-scores represent lower than expected based on the single gene  
346 knockouts independently, similar to the methodology applied in a recent survey of genetic  
347 interactions in cancer cells using multiplex CRISPR perturbation<sup>33</sup> (see Methods). Gene self-  
348 interactions (when the same gene is in the A and B position, **Figure 4d**) should therefore be  
349 negative for proliferation suppressors and positive for essentials (**Figure 4f-g, Supplementary**  
350 **Figure 6**). Overall, genetic interaction Z-scores in the two cell lines showed moderate correlation

351 (Figure 4g) and previously reported synthetic interactions between *C12orf49* and low-density  
352 lipoprotein receptor *LDLR*<sup>17</sup> and between *SREBF1* and its paralog *SREBF2*<sup>17</sup> are identified in both  
353 cell lines (Supplementary Figure 6f-g).

354  
355 In contrast with the interactions found in both cell lines, background-specific genetic interactions  
356 reflect the genotypic and phenotypic differences between the cells. The negative interaction  
357 between tumor suppressor *PTEN* and mTOR repressor *TSC1* in *PTEN*<sup>wt</sup> Nomo1 cells is  
358 consistent with their epistatic roles in the mTOR regulatory pathway. Both genes show positive  
359 knockout fitness in Nomo1 (Figure 4e) but their dual knockout does not provide an additive  
360 growth effect, resulting in a suppressor interaction with a negative Z-score (Figure 4g-h).  
361 Similarly, suppressor genetic interactions between *ACACA* and downstream proliferation  
362 suppressor genes *CHP1* and *GPAT4* are pronounced in MOLM13 cells, consistent with epistatic  
363 relationships in a linear biochemical pathway (Figure 4h). These interactions are not replicated  
364 with query gene *FASN*, but both *FASN* and *ACACA* show negative interactions with fatty acid  
365 transport gene *FABP5* and positive interactions with *SREBF1* and *SCD*, the primary desaturase  
366 of long-chain saturated fatty acids. All of these interactions are absent in Nomo1, demonstrating  
367 the rewiring of the lipid biosynthesis genetic interaction network between these two cell types  
368 (Figure 4h).

369  
370 **FASTS Signature Predicts Sensitivity to Saturated Fatty Acids**  
371  
372 The significant differences in the single- and double-knockout fitness signatures between the two  
373 cell lines suggests a major rewiring of lipid metabolism in these cells. *CHP1* and *GPAT4* are  
374 reciprocal top correlates in the Avana coessentiality network ( $r = 0.43$ ,  $P = 2.5 \times 10^{-34}$ ), strongly  
375 predicting gene co-functionality<sup>21</sup>. Two recent studies characterized the role of lysophosphatidic  
376 acid acyltransferase *GPAT4* in adding saturated acyl moieties to glycerol 3-phosphate, generating  
377 lysophosphatidic acid (LPA) and phosphatidic acid (PA), the precursors for cellular phospholipids  
378 and triglycerides, and further discovered *CHP1* as a key regulatory factor for *GPAT4* activity<sup>67,68</sup>.  
379 Within hematological cancer cell lines, the coessentiality network is significantly restructured, with  
380 the *ACACA/FASN* module correlated with *SCD* in most backgrounds ( $r = 0.35$ ,  $P < 10^{-18}$ ) but  
381 strongly anticorrelated in 36 blood cancer cell lines ( $r = -0.52$ ,  $P < 10^{-3}$ , Figure 3e). The magnitude  
382 of this change in correlation is ranked #8 out of 31 million gene pairs (see Methods). In contrast,  
383 *ACACA* and *FASN* are weakly correlated with *CHP1* in most tissues but strongly correlated in  
384 AML, with underlying covariation largely driven by the PS phenotype in FASTS cells (Figure 3e).

385 This pathway sign reversal is confirmed in the single knockout fitness observed in our screens:  
386 SCD is strongly essential in MOLM13 but not in NOMO1 (**Figure 4e**).  
387

388 Collectively these observations make a strong prediction about the metabolic processing of  
389 specific lipid species. Faster proliferation upon knockout of genes related to saturated fatty acid  
390 processing, coupled with increased dependency on fatty acid desaturase gene *SCD* (**Figure 5a**),  
391 suggests that these cells are at or near their carrying capacity for saturated fatty acids. To test  
392 this prediction, we exposed three FASTS cell lines and four other AML cell lines to various species  
393 of saturated and unsaturated fatty acids. FASTS cells showed significantly increased apoptosis  
394 in the presence of 200  $\mu$ M palmitate (**Figure 5b-c**) while no other species of saturated or  
395 unsaturated fatty acid showed similar differential sensitivity. In addition, analysis of metabolic  
396 profiles of cells in the Cancer Cell Line Encyclopedia<sup>69,70</sup> showed that saturated acyl chains are  
397 markedly overrepresented in triacylglycerol (TAG) in FASTS cells (**Figure 5d**), in contrast with  
398 other lipid species measured (**Supplementary Figure 7**). Palmitate-induced lipotoxicity has been  
399 studied in many contexts – and importantly, the role of *GPAT4* and *CHP1* in mediating lipotoxicity  
400 was well described recently<sup>67,68</sup> – but, to our knowledge, this is the first instance of a genetic  
401 signature that predicts liposensitivity.

402

#### 403 ***Prognostic signature for FASTS genes***

404

405 To explore whether the FASTS phenotype has clinical relevance, we compared our results with  
406 patient survival information from public databases. Using genetic characterization data from  
407 CCLE<sup>69</sup>, we did not find any lesion which segregated FASTS cells from other CD33+ AML cells  
408 (**Figure 6a**), so no mutation is nominated to drive a FASTS phenotype *in vivo*. Instead, we  
409 explored whether variation in gene expression was associated with patient outcomes. We  
410 included genes in the core FASTS module as well as genes with strong genetic interactions with  
411 ACACA/FASN in our screen (**Figure 6a**). To select an appropriate cohort for genomic analysis,  
412 we first considered patient age. Although AML presents across every decade of life, patients from  
413 whom FASTS cell lines were derived are all under 30 years of age (sources of other AML cells  
414 ranged from 6 to 68 years; **Figure 6b**). With this in mind, we explored data from the TARGET-  
415 AML<sup>71</sup> project, which focuses on childhood cancers (**Figure 6c**). Using TARGET data, we  
416 calculated hazard ratios using univariate Cox proportional-hazards modeling with continuous  
417 mRNA expression values for our genes of interest as independent variables. We observed that  
418 4/7 FAS genes, *GPAT4*, *CHP1*, *PCGF1*, and *GPI*, show significant, negative hazard ratios (HR),

419 consistent with a tumor suppressor signature (**Figure 6d**), and that no other gene from our set  
420 shows a negative HR. Indeed, when stratifying patients from the TARGET cohort with high  
421 expression of *GPAT4*, *CHP1*, *PCGF1*, and *GPI* (**Figure 6e**), we observe significantly improved  
422 survival (P-value = 0.001, **Figure 6f**). These findings are not replicated for *GPAT4*, *CHP1*, and  
423 *GPI* in the TCGA<sup>72</sup> or OHSU<sup>73</sup> tumor genomics data sets, possibly because they sample older  
424 cohorts (Polycomb group subunit *PCGF1* is observed to have a HR < 1 within the OHSU cohort,  
425 **Supplementary Figure 8a**). However, age is not generally associated with expression of genes  
426 in the FAS cluster in either cell lines or tumor samples (**Supplementary Figure 8**).  
427

## 428 Discussion

429  
430 CRISPR screens have had a profound impact on cancer functional genomics. While research has  
431 been mainly focused on essential gene phenotypes, there is still much clinically relevant biology  
432 that can be uncovered by examining other phenotypes from a genetic screen. We establish a  
433 methodology that can reliably identify the proliferation suppressor phenotype from whole-genome  
434 CRISPR knockout genetic screens. This represents, to our knowledge, the first systematic study  
435 of this phenotype in the more than 1,000 published screens<sup>8,10,11,13,48</sup>.  
436

437 The activity of proliferation suppressor genes is inherently context-dependent, rendering global  
438 classification difficult. As with context-dependent essential genes, the strongest signal is attained  
439 when comparing knockout phenotype with underlying mutation state. For example, wildtype and  
440 mutant alleles of classic tumor suppressor examples *TP53* and *PTEN* are present in large  
441 numbers of cell lines, enabling relatively easy discrimination of PS behavior in wildtype  
442 backgrounds, but most mutations are much more rare, reducing statistical power. Our model-  
443 based approach enables the discovery of PS phenotype as an outlier from null-phenotype  
444 knockouts. Using this approach, we recover COSMIC-annotated TSGs exhibiting the PS  
445 phenotype when wildtype alleles are expressed at nominal levels.  
446

447 Co-occurrence of proliferation suppressors follows the principles of modular biology, with genes  
448 in the same pathway acting as proliferation suppressors in the same cell lines. We observe  
449 background-specific putative tumor suppressor activity for the PTEN pathway, P53 regulation,  
450 mTOR signaling, chromatin remodeling, and others. The co-occurrence network also reveals a  
451 novel module associated with glycerolipid biosynthesis, which exhibits the PS phenotype in a  
452 subset of AML cells. Analysis of the rewiring of the lipid metabolism coessentiality network in AML

453 cells corroborated this discovery, and led us to define the Fatty Acid Synthesis/Tumor Suppressor  
454 (FASTS) phenotype in four AML cell lines. A survey of genetic interactions, using the enCas12a  
455 multiplex knockout platform, showed major network rewiring between FASTS and other AML cells  
456 and revealed strong genetic interactions in FASTS cells with *GPAT4*, a key enzyme in the  
457 processing of saturated fatty acids, and its regulator *CHP1*. Collectively these observations  
458 suggest that FASTS cells are near some critical threshold for saturated fatty acid carrying  
459 capacity, which we validated biochemically by treatment with fatty acids and bioinformatically  
460 through analysis of CCLE metabolomic profiles.

461

462 Confirming the clinical relevance of an *in vitro* phenotype can be difficult. No obvious mutation  
463 segregates FASTS cells from other AML cells, and with only four cell lines showing the FASTS  
464 phenotype, we lack the statistical power to discover associations in an unbiased way. However,  
465 by narrowing our search to strong hits from the differential network analyses, we found a  
466 significant survival advantage in a roughly age-matched cohort for *GPAT4* and *CHP1*  
467 overexpression. This finding points to a wholly novel tumor suppressor signature for our PSG  
468 module, though significant further study is necessary to determine whether this gene expression  
469 signature confers a similar *in vivo* metabolic rewiring and sensitivity to saturated lipids.

470

471 The combination of genetic, biochemical, and clinical support for the discovery of a novel tumor  
472 suppressor module has several implications. First, it provides a clinical signature that warrants  
473 further research as a prognostic marker as well as a potential therapeutic target. Second, it  
474 demonstrates the power of differential network analysis, and in particular differential genetic  
475 interaction networks, to dissect the rewiring of molecular pathways from modular phenotypes.  
476 And finally, it suggests that there still may be much to learn from data-driven analyses of large-  
477 scale screen data, beyond the low-hanging fruit of lesion/vulnerability associations.

478

479

480

481

482 **Acknowledgments**

483

484 This research was performed in partial fulfillment of the requirements for the PhD degree from  
485 The University of Texas MD Anderson Cancer Center UTHealth Graduate School of Biomedical  
486 Sciences; The University of Texas MD Anderson Cancer Center, Houston, Texas 77030. WFL,  
487 MMc, MMo, and TH were supported by NIGMS grant R35GM130119. MC is supported by a  
488 Kopchick fellowship and Pauline Altman-Goldstein Foundation Discovery Fellowship. EK is  
489 supported by a grant from the Prostate Cancer Foundation. MD is supported by a Schissler  
490 Foundation fellowship. TH is a CPRIT Scholar in Cancer Research (RR160032), and is  
491 additionally supported by MD Anderson Cancer Center Support Grant P30 CA016672. WFL is  
492 supported by the American Legion Auxiliary Fellowship in Cancer Research. This work was  
493 supported by the Andrew Sabin Family Foundation Fellowship (TH). Flow cytometry was  
494 performed at MDACC's Advanced Cytometry & Sorting Facility supported by the NCI Cancer  
495 Center Support Grant P30CA16672.

496

497 **Author Contributions**

498

499 WFL performed all PS discovery analysis. MF, AG, AS performed genetic interaction screens and  
500 PD, MC performed bioinformatic analysis. WFL, MC, EK, and MD performed all other  
501 bioinformatic analysis. MMo and MMc performed lipid profiling experiments. JGD and TH  
502 supervised the research. WFL and TH drafted the manuscript and all authors edited it.

503

504 **Competing Interests**

505

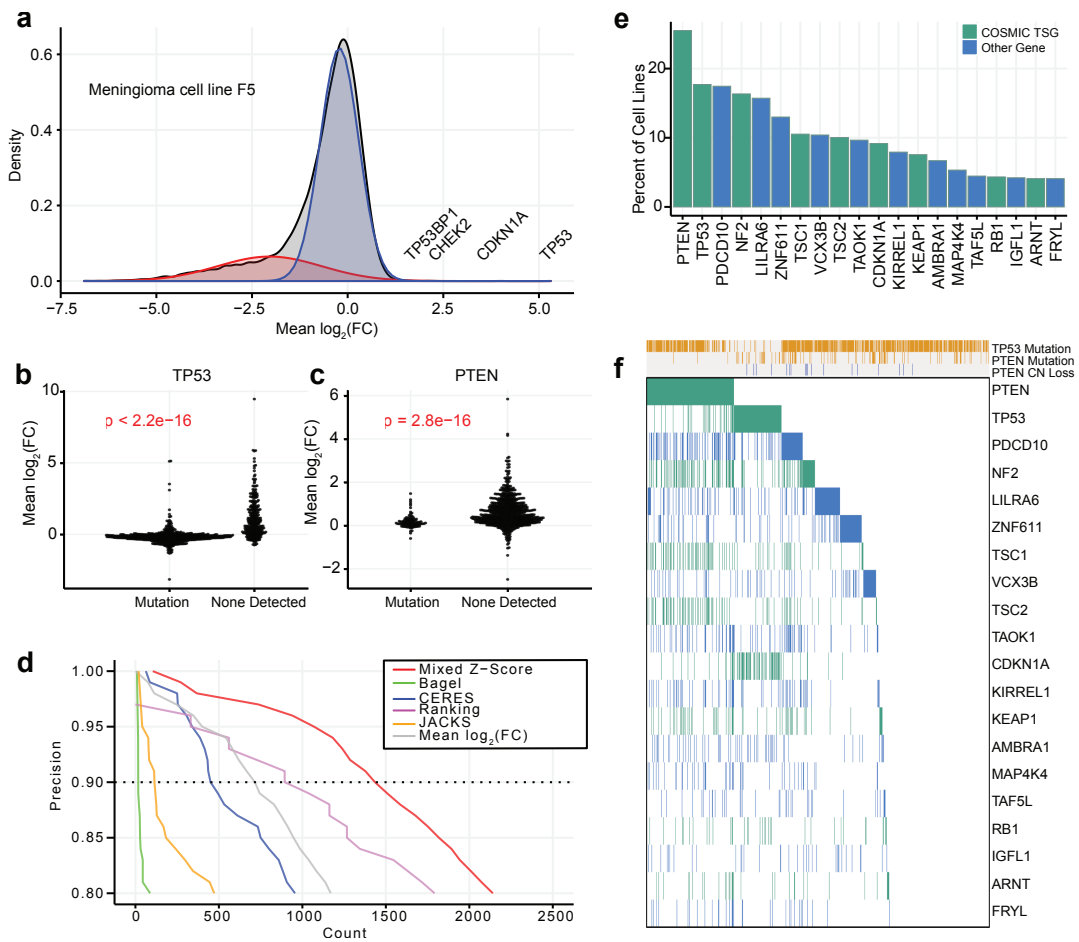
506 JGD consults for Agios, Maze Therapeutics, Microsoft Research, and Pfizer; JGD consults for  
507 and has equity in Tango Therapeutics. WFL is a former consultant for BioAge Labs, and has  
508 equity in Kronos Bio Inc.

509

510

511 **Figure Legends**

512

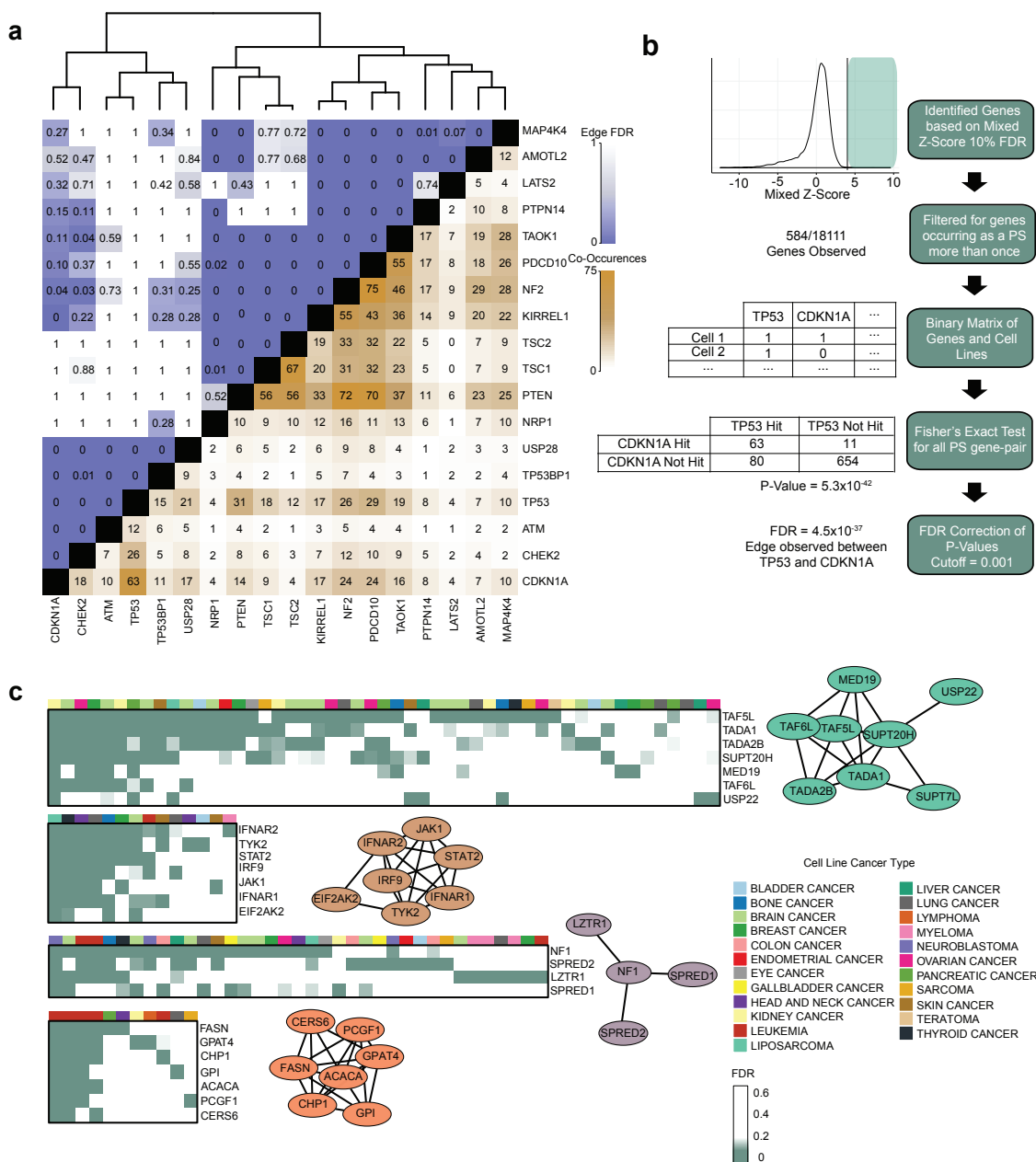


513

514

515 **Figure 1. Discovery of Proliferation Suppressor genes.** (a) Fold-change distribution of a  
516 typical CRISPR knockout screen has a long left tail of essential genes, and a small number of  
517 genes whose knockout increases fitness (proliferation suppressor genes, “PSG”). A two-  
518 component Gaussian mixture model (red, blue) models this distribution. (b) and (c) Fold change  
519 of common tumor suppressors across 808 cell lines (P-values, Wilcoxon rank-sum tests). (d)  
520 Precision vs. recall of mixed Z-score and other CRISPR analysis methods. Dashed line, 90%  
521 precision (10% FDR). (e) Fraction of cell lines in which known tumor suppressors (green) or other  
522 genes (blue, not defined as TSG by COSMIC) are classified as PS genes at 10% FDR. (f)  
523 Presence of each known TSG across 808 cell lines, vs. cell genetic background. Gold, mutation  
524 present; gray, absent. Green or blue, following color scheme in (e), gene is classified as a  
525 proliferation suppressor.

526

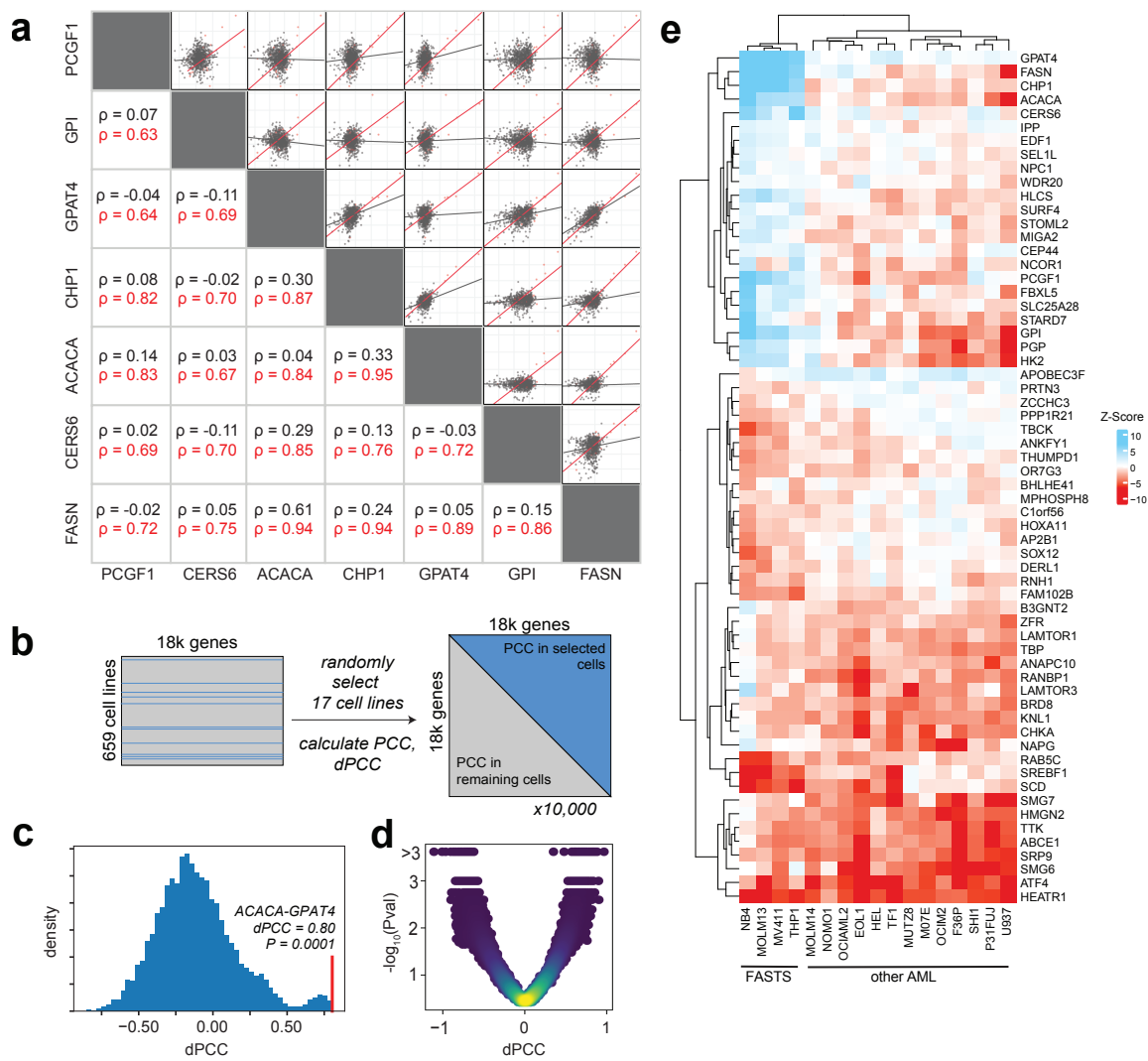


527

528

529

530 **Figure 2. Co-occurrence of PSG.** (a) Co-occurrence/mutual exclusivity of common TSG as PSG  
531 in CRISPR screens. Brown, number of cell lines in which two genes co-occur as PSG at 10%  
532 FDR. Blue, FDR of co-occurrence. Hierarchical clustering delineates functional modules. (b)  
533 Pipeline for building the co-PS network. (c) Examples from the Co-PS network. Nodes are  
534 connected by edges at FDR < 0.1%. Heatmaps indicate presence of PSG vs. cell lineage.  
535



538 **Figure 3. Differential network analysis of fatty acid synthesis module.** (a) Among genes in  
539 the FAS module, Pearson correlation coefficients of shuffled Z score profiles are substantially  
540 higher in AML cells (red) than in other cells (gray). (b) Significance testing of differential PCC  
541 (dPCC) involves quality filtering of Avana data (n=659 cell lines, including 17 AML cell lines),  
542 building a null distribution by randomly selecting 17 cell lines, and calculating PCC between all  
543 gene pairs in the selected cells and the remaining cells. (c) After 1,000 repeats, a null distribution  
544 is generated for each pair, and a two-sided P-value is calculated for the observed AML-vs-other  
545 dPCC. (d) Volcano plot of dPCC vs. P-value for all genes in the Co-PS cluster. (e) Heatmap of  
546 mixed Z score for 17 AML cell lines in selected genes with high |mixed Z| and high |dPCC|.  
547 Clustering of cell lines indicates the putative Fatty Acid Synthesis/Tumor Suppressor (FASTS)  
548 subtype.

549

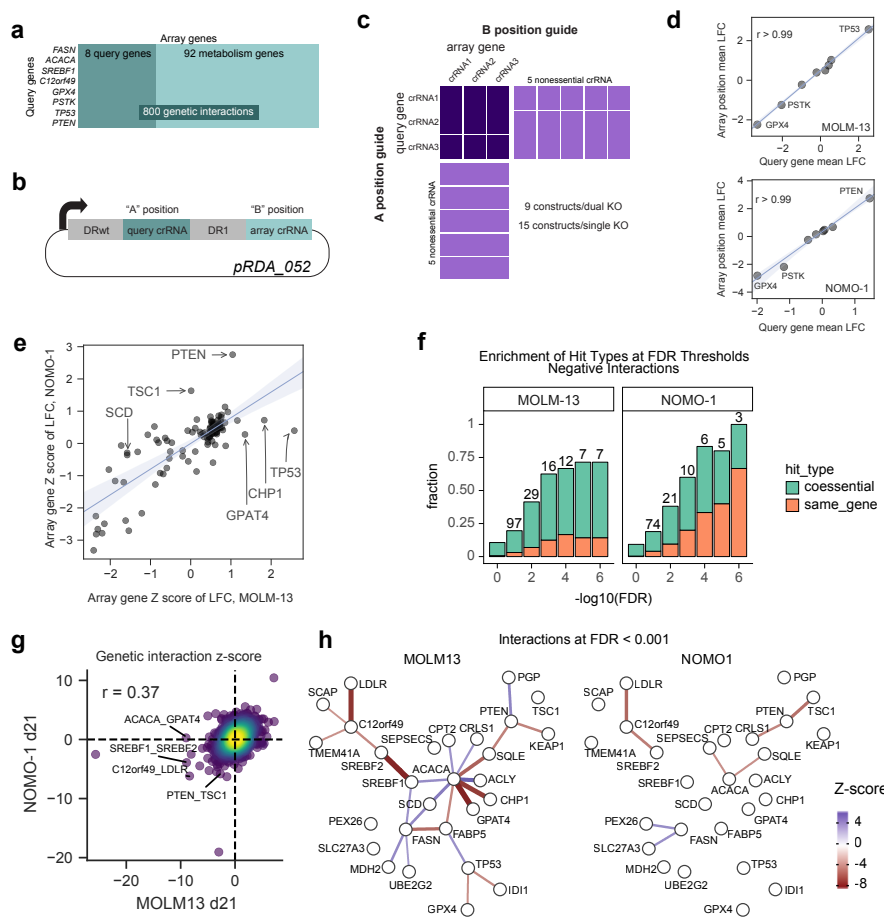


Figure 4

552 **Figure 4. Genetic interactions reveal a rewired lipid biosynthesis pathway in FASTS cells.**  
553 (a) Genetic interaction screen targets 8 query genes, selected from FASTS cluster and dPCC  
554 analysis, and 100 array genes sampling lipid metabolism pathways, for a total of 800 pairwise  
555 knockouts. (b) Library design uses a dual-guide enCa12a expression vector which targets the  
556 query gene in the “A” position and array gene in the “B” position. (c) Overall library design includes  
557 three crRNA/gene plus control crRNA targeting nonessential genes. Single-knockout constructs  
558 (target gene paired with nonessential controls) allow accurate measurement of single knockout  
559 fitness. (d) Considering single knockout fitness of query genes in the “A” and “B” position of the  
560 crRNA expression vector shows no position effects in the two cell lines screened (MOLM13,  
561 NOMO1). LFC, log fold change. (e) Single knockout fitness (Z-score of mean LFC) is highly  
562 consistent between MOLM13 and NOMO1, but reveals background-specific PS genes. (f)  
563 Enrichment among GI for coessential and self-interacting genes. Self-interactions among genes  
564 that show single knockout fitness phenotypes are expected, reflecting quality of GI observations.  
565 (g) Global comparison of MOLM13, NOMO1 genetic interaction Z scores. (h) Network view of  
566 interactions in each background shows rewiring in MOLM13 FASTS cells.

567

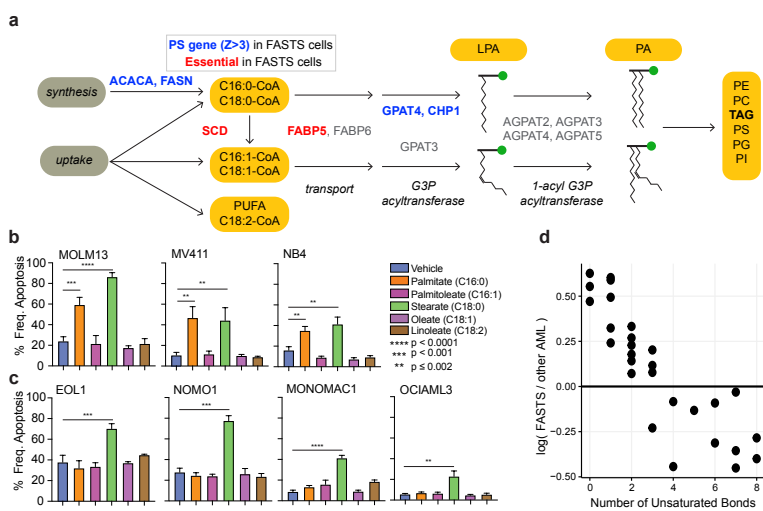


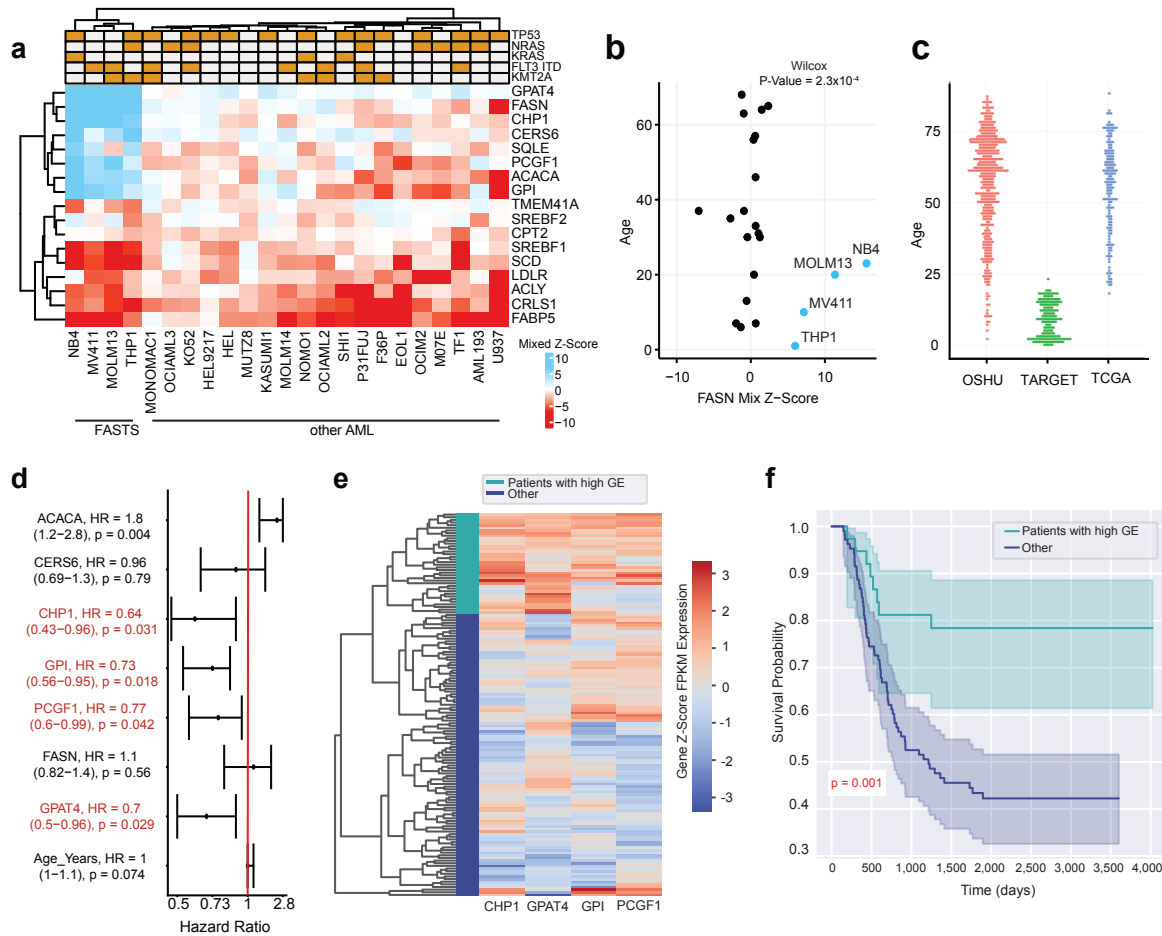
Figure 5

568

569

570

571 **Figure 5. FASTS cells are sensitive to saturated FA.** (a) Schematic of the fatty acid/glycerolipid  
572 synthesis pathway. Blue, PSG in FASTS cells. Red, essential genes. Pathway analysis suggests  
573 saturated fatty acids are a critical node. (b) Apoptosis of FASTS cells in response to media  
574 supplemented with 200  $\mu$ M fatty acids. All three cell lines show marked sensitivity to palmitate.  
575 (c) Apoptosis of other AML cells in response to fatty acids shows no response to palmitate. (d)  
576 Triacylglycerol (TAG) species metabolite differences. The x axis represents the median difference  
577 of log10 normalized peak area of the metabolite in FASTS cells vs all other AML cells. The y axis  
578 represents the number of saturated bonds present. Each dot represents a unique metabolite.  
579



583 **Figure 6. Prognostic signature of FAS module.** (a) Heatmap of mixed Z scores for genes  
584 implicated in the genetic interaction network. Top, common AML lesions. (b) Mixed Z-score of  
585 FASN in AML cell lines vs. age of patient from which cell lines were derived. Blue, FASTS cells.  
586 (c) Age distribution of AML patients in three public tumor genomics cohorts. (d) Hazard ratios  
587 (95% CI; univariate Cox proportional hazards test) for expression of genes in (a), using genomics  
588 and survival data from TARGET. (e) Hierarchical clustering of gene expression in TARGET, using  
589 the four genes with negative HR. Green, high expression cluster. Blue, others. (F) Kaplan-Meier  
590 survival analysis of AML patients in TARGET, comparing patients in high expression cluster vs.  
591 others.  
592

593 **Supplementary Materials and Methods**

594

595 **Code Availability**

596

597 Mixed Z-scoring, analysis using scoring metric, co-occurrence network, and survival analysis was  
598 conducted in R version 4.0.4<sup>74,75</sup>. dPCC correlation analysis, including empirical calculations were  
599 conducted in Python 3.8.2<sup>76</sup>, using the packages SciPy<sup>77</sup>, NumPy<sup>78</sup>, Matplotlib<sup>79</sup>, and pandas<sup>80</sup>.  
600 Code is made available at: [https://github.com/hart-lab/tsg\\_crispr\\_screen\\_survey/](https://github.com/hart-lab/tsg_crispr_screen_survey/). R packages  
601 tidyverse<sup>81</sup>, data.table<sup>82</sup>, and knitr<sup>83-85</sup> were used for figure generation, data manipulation, and  
602 general R functions; mixtools<sup>86</sup>, permute<sup>87</sup>, and PRROC<sup>88,89</sup> were used for data simulations  
603 present in figures and evaluation; biomaRt<sup>90,91</sup>, and org.Hs.eg.db<sup>92</sup> were used in integrating data  
604 types; cowplot<sup>93</sup>, ggbeeswarm<sup>94</sup>, annotate<sup>95</sup>, RColorBrewer<sup>96</sup>, ComplexHeatmap<sup>97</sup>, gplots<sup>98</sup>,  
605 ggpubr<sup>99</sup>, grid<sup>75</sup>, circlize<sup>100</sup>, ggthemes<sup>101</sup>, ggExtra<sup>102</sup>, patchwork<sup>103</sup>, and ggplot2<sup>104</sup>, were used for  
606 figure aesthetics and generation. R packages survival<sup>105,106</sup> and survminer<sup>107</sup> were used for  
607 survival analysis and figure generation. Analysis related to Kaplan Meier and patient  
608 stratification was done in python version 3.8.5<sup>108</sup> using the packages pandas<sup>80</sup>, numpy<sup>78</sup>, and  
609 scipy<sup>77</sup> for statistical functions and data manipulation, seaborn<sup>109</sup>, plotly<sup>110</sup>, and matplotlib<sup>79</sup>  
610 for figure aesthetics and generation, and lifelines<sup>111</sup> for both statistical analysis and figure  
611 generation.

612

613

614 Analysis of enCas12a multiplex genetic screens was conducted in R 4.0.0 and Python 3.8.3<sup>112</sup>.  
615 Code for this analysis is available at <https://github.com/PeterDeWeirdt/FASTS>. R packages  
616 tidyverse<sup>81</sup> and tidygraph<sup>113</sup> were used for data manipulation and ggraph<sup>114</sup> was used for graph  
617 visualization. Python packages SciPy<sup>77</sup>, NumPy<sup>78</sup>, Matplotlib<sup>79</sup>, pandas<sup>80</sup>, statsmodels<sup>115</sup>,  
618 plotnine<sup>116</sup> were used for analysis and visualization. The Custom package gnt<sup>117</sup> was used to  
619 calculate genetic interaction scores and ggplot<sup>118</sup> was used to generate point density plots.

620

621 **Processing DepMap Screen and CCLE Genomics Data**

622

623 Raw read count data and a map of guide RNAs were downloaded from the DepMap database  
624 ([www.depmap.org](http://www.depmap.org))<sup>10,48</sup> and Project Score database (<https://depmap.sanger.ac.uk/>)<sup>13</sup>. Avana data  
625 version 2020q4<sup>49</sup> was used for this analysis. To avoid genetic interaction effects, we discarded  
626 sgRNAs targeting multiple protein coding genes annotated as public or update pending in The

627 Consensus Coding Sequence (CCDS, release 22)<sup>119</sup>. Gene names in the guide RNA maps of  
628 Avana and Project Score were updated using human gene information obtained from ncbi ftp.  
629 Then, read count data for each replicate was passed through CRISPRcleanR<sup>120</sup> with location  
630 information of sgRNAs for the Avana CRISPR library based on GENCODE<sup>121</sup> to correct depletion  
631 effects caused by copy-number amplification. Following this correction, each guide's log<sub>2</sub> fold-  
632 change was calculated. For Project Score data, we used only the gene location information of KY  
633 library v1.0 which is built in CRISPRcleanR. Normalized TPM RNA-seq data, copy number data,  
634 and mutation annotations for CCLE<sup>69</sup> cells were also downloaded from DepMap. Ensembl gene  
635 id in RNA-seq data was converted to gene symbol using cross reference downloaded from  
636 Ensembl Biomart<sup>122</sup>.

637

### 638 **Mixed Z-Score Metric**

639

640 Mixed z-score metric was generated using R version 4.0.4 base stat packages<sup>75</sup> and the  
641 mixtools<sup>86</sup> normalmixEM function. To calculate the mixed z-score, individual guide log<sub>2</sub> fold-  
642 changes for each cell line were passed through the default settings of the normalmixEM function  
643 to fit two distinction normal distributions. Of the 808 cell lines passed through this analysis, 805  
644 cell lines were able to converge with two distinction normal distribution following 1,000 iterations.  
645 The calculated mean and standard deviation of the higher (more positive) distribution were  
646 recorded. Along with the uncorrected original gene log<sub>2</sub> fold-change, was used to calculate the  
647 corresponding mixed z-score. The original and mixed Z-score formula is as follows:

648 
$$\text{Mixed Gene Z - Score} = \frac{x - \mu_{high}}{\sigma_{high}}$$

649 Where  $x$  is the original gene log<sub>2</sub> fold-change,  $\mu_{high}$  is the average of the more positive fitted  
650 distribution, and  $\sigma_{high}$  is the standard deviation of the more positive fitted distribution. This metric  
651 was calculated for the DepMap 2020q4<sup>49</sup> screen set, and the Sanger's DepMap<sup>13</sup> screen set for  
652 **Supplementary Figure 3**.

653

### 654 **Comparisons of Fitness Scoring Metrics**

655

656 The following describes our comparative analysis of screening algorithms observed in  
657 **Supplementary Figure 1**. JACKS<sup>43</sup> and BAGEL<sup>41,42,123</sup>, software was downloaded from their  
658 corresponding GitHub official distribution sites: <https://github.com/felicityallen/JACKS>, and  
659 <https://github.com/hart-lab/bagel>. We ran JACKS and BAGEL with raw fold change data of

660 DepMap 2020q4 version<sup>49</sup>, gene guide map and replicate information. We obtained DepMap  
661 2020q4 CERES scores from ‘dependency\_score.csv’ downloaded from DepMap depository.  
662 Ranking was performed per screen and based on mean  $\log_2$  fold-change values per gene.

663  
664 We used the cancer gene census (CGC) list from COSMIC<sup>45,46</sup> to compare fitness methods that  
665 can detect proliferation suppressor activity. Tumor suppressor genes (TSGs) from CGC represent  
666 a gene set of well-known proliferation suppressors. We separated the CGC gene list in two gene  
667 sets, genes with any tumor suppressor role in cancer representing true positive proliferation  
668 suppressor observations, and genes with any oncogene role in cancer representing false  
669 positives. Additionally, we added reference non-essential genes<sup>7,47</sup> to the false positive list as  
670 these genes are not expected to demonstrate any phenotype. With these compiled lists, we  
671 evaluated each metric’s fitness scores, to see which metric would best separate the true and false  
672 positive gene lists. The R package PRROC was used for fitness scoring evaluation<sup>88,89</sup>.  
673

#### 674 **Direct Proliferation Suppressor Comparisons of Avana and Sanger Screen Datasets**

675  
676 The CRISPRcleanR<sup>120</sup> corrected fold-change Sanger screen set<sup>13</sup> was pushed through identical  
677 pipelines used to calculate the mixed z-score metric. Quality analysis of the mixed z-score metric  
678 for both data sets was pushed using identical gene sets described in the “Comparisons of Fitness  
679 Scoring Metrics” section. This analysis was restricted to only overlapping cell lines, 186 total, in  
680 both datasets.

681  
682 The fitness enhancement introduced by PSG knockout, relatively weak compared to severe  
683 defects from essential gene knockout, often precludes detection in a shorter experiment. In the  
684 example F5 cell line (**Figure 1a**), a 2.5-fold change over a 21-day time course corresponds to a  
685 fitness increase of only ~12% for rapidly growing cells, or a doubling time decrease from 24 to 21  
686 hours. In a 14-day experiment, this increased proliferation rate would result in an observed log  
687 fold change of only ~1.7, within the expected noise from genes with no knockout phenotype. This  
688 is explained in detail as follows:

689  
690 **Theoretical Fold-Change and Growth Rate Quantification:** To assess hypothetical differences  
691 of proliferation suppressor fitness scoring metrics based on standard sampling times of screen  
692 collection taken from the Sanger and Avana databases<sup>10,11,13,48</sup>, we calculated theoretical cell

693 population differences of wild-type and knocked out proliferation suppressor cell lines. The  
694 following formula can be used to calculate cell populations based on doubling rate per day:

695

696 
$$X_f = X_i * 2^{k*t}$$

697

698 In this formula  $X_f$  is the final population number of cells,  $X_i$  is the initial population of cells,  $k$  is  
699 doubling time of the cells (in days), and  $t$  is time in days. In order to compare cells we can assume  
700 that these formulas are consistent with both wild-type cells and knocked out proliferation  
701 suppressor cells. With, knocked out proliferation suppressor cells the assumption is that these  
702 cells would grow faster compared to wild-type conditions and thus  $k_{ps} > k_{wt}$ , where  $k_{ps}$  is the growth  
703 rate for proliferation suppressor knocked out cells, and  $k_{wt}$  is the growth rate of wild type cells.  
704 These two independent growth rates are related as:

705

706 
$$k_{ps} = k_{wt} + \Delta k$$

707

708  $\Delta k$  represents the change in growth rate resulting from genetic knockout, and is assumed to be  
709 positive. The growth rate formula for wild-type and proliferation suppressor cells is thus:

710 
$$X_{wt} = X_i * 2^{k_{wt}*t}, X_{ps} = X_i * 2^{(k_{wt}+\Delta k)*t}$$

711

712 We then solved for  $\Delta k$ , with  $\text{Log}_2(X_{ps}/X_{wt})$  as  $\text{Log}_2(FC)$ , representing the fold-change difference  
713 between the cell populations at time  $t$ :

714

715 
$$\text{Log}_2 FC = \text{Log}_2 \left( \frac{X_{ps}}{X_{wt}} \right)$$

716

717 
$$\text{Log}_2 FC = \text{Log}_2 \left( \frac{X_i * 2^{(k_{wt}+\Delta k)*t}}{X_i * 2^{k_{wt}*t}} \right)$$

718

719 
$$\text{Log}_2 FC = \text{Log}_2 \left( \frac{2^{(k_{wt}+\Delta k)*t}}{2^{k_{wt}*t}} \right)$$

720

721 
$$\text{Log}_2 FC = ((k_{wt} + \Delta k) * t) - (k_{wt} * t)$$

722

723 
$$\text{Log}_2 FC / t = k_{wt} + \Delta k - k_{wt}$$

724

725  $\text{Log}_2\text{FC}/t = \Delta k$

726

727 For a representative  $\text{Log}_2(\text{FC})$  of 2.5, which represents a sizable gain in fitness from a knocked-  
728 out proliferation suppressor, and  $t = 21$  days, representing the time in which the Avana screens  
729 were sampled, we calculated  $\Delta k$ :

730

731  $\Delta k = \frac{2.5}{21} = 0.12$

732

733 Using the calculated  $\Delta k$  at 0.12, we can calculate the hypothetical  $\text{Log}_2(\text{FC})$  that would be  
734 expected at  $t = 14$  days, representing the time in which the Sanger screens were sampled:

735

736  $\text{Log}_2\text{FC} = \Delta k * t$

737

738  $\text{Log}_2\text{FC} = 0.12 * 14 = 1.7$

739

740 The resulting theoretical measurements demonstrate that  $\Delta k$  can be identical between two  
741 samples, however the time in which the sample was taken will influence the ratio between the two  
742 measured cell populations. Taken together, this demonstrates that samples at shorter time points  
743 will demonstrate smaller quantified population size differences between wild-type and proliferation  
744 suppressor knocked out cells compared to samples taken at longer time points.

745

## 746 **Proliferation Suppressor Co-Occurrence Network**

747

748 The co-occurrence network was developed based on FDR-corrected P-values from Fisher exact  
749 tests of all gene by gene comparisons that were identified as a proliferation suppressor more than  
750 once (584 genes total). Parallel processing, Fisher's exact test, Benjamini & Hochberg FDR p-  
751 value adjustment were done using base R stat packages<sup>75</sup>. **Figure 2a** was created with heatmap.2  
752 function from the R gplots<sup>98</sup> package, with the dendrogram created through base R<sup>75</sup> functions of  
753 euclidean distance, and complete agglomeration methods clustering of the Fisher's exact test  
754 score between gene pairs. Smaller heatmaps displayed in **Figure 2c** were made using the R  
755 ComplexHeatmap library<sup>97</sup>. Network visualization was completed using Cytoscape<sup>124</sup>.

756

757 Network creation followed the corresponding steps; **1)** Identify all proliferation suppressor  
758 observations at a 10% FDR threshold ( $Z \geq 3.83$ ). **2)** Filter for gene proliferation suppressor  
759 observations that occurred at least 2 or more times, selecting for a total of 584 out of 18,111  
760 genes available (3.2% total available genes); **3)** Create a binary (1 = proliferation suppressor, 0  
761 = not proliferation suppressor) matrix of all 584 genes in all cell lines; **4)** Conducted Fisher's exact  
762 test of every possible 2 x 2 contingency table of the 584 selected genes (n= 170,236 tests); and  
763 **5)** Adjust the corresponding p-values to FDR values, using a cutoff of 0.001 (0.1% FDR) to define  
764 edges. By assessing gene edges through Fisher exact-tests, we observe gene associations that  
765 are based on the relative proportion of co-occurrences between two genes.

766

767

### 768 **Proliferation Suppressor Network Enrichment**

769

770 To test network enrichment of observed edges (**Supplementary Figure 4a**), we took 10,000  
771 random samples of 462 (total number of edges in the co-occurrence network) gene pairs from the  
772 170,236 available all by all gene pair Fisher's exact test set. We then compared each sample to  
773 see the frequency of gene pairs observed to have some interaction within HumanNet<sup>61</sup>, excluding  
774 genetic interactions observed solely in the co-essentiality network component<sup>21</sup> (generated from  
775 the same data) to prevent circularity. Additionally, we compared our selected mixed Z-Score cutoff  
776 against other various Z-Score cutoffs to ensure that we observed appropriate edge representation  
777 from HumanNet (**Supplementary Figure 4b**). Networks were made using identical pipelines and  
778 Fisher's exact test set cutoffs with Z-Score cutoffs between 3 and 8 at 0.2 increments.

779

### 780 **Differential Pearson Correlation Coefficient Analysis**

781

782 Differential Pearson correlation coefficient (dPCC) analysis was conducted to identify genetic  
783 fitness distinctions between AML cells and all other cells (**Figure 3**). Initial correlations (**Figure**  
784 **3a**) of FAS cluster genes, PCGF1, CERS6, GPI, FASN, CHP1, GPAT4, and ACACA were  
785 calculated with R version 4.0.4 base stat packages<sup>75</sup> and plotted in ggplot2<sup>104</sup>.

786

787 Following this observation, a follow up dPCC analysis was conducted on the FASTS cluster genes  
788 to assess dPCC quality. Cell line screens with low quality (Cohen's D < 2.5 or recall of known  
789 core essential genes < 60%) were excluded, leaving 659 cell lines. Following this filtering step,  
790 two gene-by-gene correlation matrices were calculated. The first correlation matrix calculated all

791 gene by gene pairs in only the available AML cell lines (n=17). The second matrix calculated all  
792 gene by gene pairs in the remaining 642 cell lines. The dPCC matrix is therefore the AML  
793 correlation matrix minus the non-AML correlation matrix.

794

795 Each gene-pair has a unique joint distribution of mixed Z scores; thus, the significance of each  
796 dPCC score must be calculated individually. To do this, we generated null distributions for dPCC  
797 for each gene pair. We took random selections without replacement of 17 cell lines (matching the  
798 n of AML cells), calculated all gene by gene pairwise correlations within this selection and within  
799 the remainder, and calculated dPCC. We repeated this sampling and calculation 1,000 times to  
800 generate a unique null distribution of dPCC for each gene pair and calculated an appropriate P-  
801 value for the observed dPCC above (right tailed for positive dPCC, left tailed for negative dPCC).

802

803 Genes which showed significant knockout phenotype ( $|mixed Z| > 5$ ) and AML-specific change in  
804 correlation (dPCC  $P < 0.001$ ) with a gene in the connected clique in the co-occurrence cluster  
805 (*CHP1, GPAT4, ACACA, FASN, GPI, CERS6, PCGF1*) were selected for further analysis (**Figure**  
806 **3e**). **Figure 3e** was made using the R ComplexHeatmap library<sup>97</sup>. **Figure 3c-d** plots were made  
807 using the Python package Matplotlib<sup>79</sup>.

808

#### 809 **Cell culture for Genetic Screens**

810

811 MOLM13 and NOMO1 cells screened with the Cas12a-mediated genetic interaction library at the  
812 Broad Institute were obtained from the Cancer Cell Line Encyclopedia.

813

814 All cell lines were routinely tested for mycoplasma contamination and were maintained without  
815 antibiotics except during screens, when the media was supplemented with 1%  
816 penicillin/streptomycin. Cell lines were kept in a 37 °C humidity-controlled incubator with 5.0%  
817 carbon dioxide and were maintained in exponential phase growth by passaging every 2-3 days.  
818 The following media conditions and doses of polybrene, puromycin, and blasticidin, respectively,  
819 were used:

820 MOLM13: RPMI + 10% FBS; 8  $\mu$ g mL<sup>-1</sup>; 4  $\mu$ g mL<sup>-1</sup>; 8  $\mu$ g mL<sup>-1</sup>

821 NOMO1: RPMI + 10% FBS; 8  $\mu$ g mL<sup>-1</sup>; 1  $\mu$ g mL<sup>-1</sup>; 8  $\mu$ g mL<sup>-1</sup>

822

#### 823 **Pooled screens**

824

825 Cell lines stably expressing enCas12a (pRDA\_174, Addgene 136476) were transduced with  
826 guides cloned into the pRDA\_052 vector (Addgene 136474) in two cell culture replicates at a low  
827 MOI (~0.5). Transductions were performed with enough cells to achieve a representation of at  
828 least 750 cells per guide construct per replicate, taking into account a 30–50% transduction  
829 efficiency. Throughout the screen, cells were split at a density to maintain a representation of at  
830 least 1000 cells per guide construct, and cell counts were taken at each passage to monitor  
831 growth. Puromycin selection was added 2 days post-transduction and was maintained for 5 days.  
832 14 days and 21 days after transduction, cells were pelleted by centrifugation, resuspended in  
833 PBS, and frozen promptly for genomic DNA isolation.

834

835

### 836 **Genomic DNA isolation and PCR**

837

838 Genomic DNA (gDNA) was isolated using the KingFisher Flex Purification System with the Mag-  
839 Bind® Blood & Tissue DNA HDQ Kit (Omega Bio-Tek #M6399-01) as per the manufacturer's  
840 instructions. The gDNA concentrations were quantitated by Qubit. For PCR amplification, gDNA  
841 was divided into 100 µL reactions such that each well had at most 10 µg of gDNA. Per 96 well  
842 plate, a master mix consisted of 144 µL of 50x Titanium Taq DNA Polymerase (Takara), 960 µL  
843 of 10x Titanium Taq buffer, 768 µL of dNTP (stock at 2.5mM) provided with the enzyme, 48 µL of  
844 P5 stagger primer mix (stock at 100 µM concentration), 480 µL of DMSO, and 1.44 mL water.  
845 Each well consisted of 50 µL gDNA plus water, 40 µL PCR master mix, and 10 µL of a uniquely  
846 barcoded P7 primer (stock at 5 µM concentration).

847

848 PCR cycling conditions: an initial 1 min at 95 °C; followed by 30 s at 94 °C, 30 s at 53 °C, 30 s at  
849 72 °C, for 28 cycles; and a final 10 min extension at 72 °C. PCR primers were synthesized at  
850 Integrated DNA Technologies (IDT). PCR products were purified with Agencourt AMPure XP  
851 SPRI beads according to manufacturer's instructions (Beckman Coulter, A63880).

852

853 Samples were sequenced on a HiSeq2500 Rapid Run flowcell (Illumina) with a custom primer of  
854 sequence: 5'-CTTGTGGAAAGGACGAAACACCGGTAATTCTACTCTTGTAGAT. The first  
855 nucleotide sequenced with the primer is the first nucleotide of the guide RNA, which will contain  
856 a mix of all four nucleotides, and thus staggered primers are not required to maintain diversity  
857 when using this approach. Reads were counted by alignment to a reference file of all possible

858 guide RNAs present in the library. The read was then assigned to a condition (e.g. a well on the  
859 PCR plate) on the basis of the 8 nt index included in the P7 primer.

860

## 861 Scoring Genetic Interactions

862

863 To score genetic interactions we used a custom python package, gnt<sup>117</sup>, available on the python  
864 package index. We use log-fold changes (LFCs) as inputs to the scoring pipeline. We define  $y_{ij}$  as  
865 the observed LFC of a guide pair  $i, j$  and  $\widehat{y}_{ij}$  as this pair's expected LFC. We then calculate the  
866 residual  $y_{ij} - \widehat{y}_{ij}$  to generate an interaction score. To define expected LFCs,  $\widehat{y}_{ij}$  we fit a linear  
867 regression for each guide,  $i$ , saying

868 
$$\widehat{y}_i = m_i \cdot x + b_i,$$

869 where  $x$  is the LFC of each guide individually and  $m_i$  and  $b_i$  are the fit slope and intercept for  
870 guide  $i$  (**Supplementary Figure 6b**). We refer to  $i$  as the anchor guide and its pairs as target  
871 guides. We then Z-score residuals within each anchor guide. This approach is similar to the one  
872 taken by Horlbeck *et al.*<sup>33</sup>.

873 To aggregate interaction scores at the gene level, we sum the z-scored residuals,  $z_{ij}$ , for all  
874 constructs  $i, j$  targeting the gene pair  $I, J$ , fixing  $I$  as the anchor gene, and divide by the square  
875 root of the number of constructs targeting  $I, J$ . We repeat this calculation, fixing  $J$  as the anchor  
876 gene. We sum scores for both of these orientations and divide by  $\sqrt{2}$  to arrive at a gene level Z-  
877 score.

878

## 879 Cell Culture for Fatty Acid Response

880

881 Human cancer cell lines used at MD Anderson were obtained as follows: EOL1, MONOMAC1,  
882 NB4, OCIAML3 (DSMZ); MOLM13 and NOMO1 (Fisher); MV411 (ATCC). Identities were  
883 confirmed upon receipt and prior to experiments by STR typing (MDACC Characterized Cell Line  
884 Core). Absence of mycoplasma was confirmed monthly (Invivogen). All cell lines were grown at  
885 37 °C in 5% CO<sub>2</sub> in low attachment flasks (Greiner) and maintained at less than 1M cells ml<sup>-1</sup>. All  
886 but one line were cultured in RPMI-1640 with 25 mM HEPES (Sigma) supplemented with 10%  
887 FBS (Sigma), 2 mM Glutamax (Gibco), 1 mM sodium pyruvate (Gibco), 10,000 units ml<sup>-1</sup> penicillin  
888 (Sigma), 10 mg ml<sup>-1</sup> streptomycin (Sigma) and 100 µg ml<sup>-1</sup> Normocin (Invitrogen). Complete

889 medium was additionally supplemented with 0.1 mM non-essential amino acids (Gibco) for  
890 MONOMAC1.

891

## 892 **Fatty Acid Solutions**

893

894 Fatty All chemicals were purchased from Sigma (St. Louis, MO). Solutions were prepared  
895 according to Luo *et al.*<sup>125</sup> following best practices<sup>126</sup>. Fatty acid stock solutions were prepared in  
896 100% ethanol at 50 mM for stearic acid or 200 mM for the rest. Fatty acid free bovine serum  
897 albumin (FAF-BSA) was dissolved in tissue culture grade (pyrogen free) water at 1.5 mM (10%  
898 w/v), filtered using 0.1 µm PES vacuum unit (Corning) and aliquoted for storage at -20°C. Ethanol  
899 stock solutions were diluted to 4 mM in FAF-BSA (molar ratio 2.7:1) and mixed gently at room  
900 temperature for 2 hours to facilitate conjugation. A vehicle control was prepared by diluting 100%  
901 ethanol in FAF-BSA to match the ethanol concentration in the 4 mM stearic acid solution. Vehicle  
902 or 4 mM solutions were aliquoted and stored at -80°C for up to 3 months. After thawing, aliquots  
903 were diluted 1:10 with complete medium to 400 µM, stored at 4°C and used within one week.

904

905

## 906 **Apoptosis Assay**

907

908 Cells were seeded 24 hr prior to treatment in 500 µL complete medium in 24-well low attachment  
909 plates (Greiner) at 250,000 cells well<sup>-1</sup>. Quadruplicate wells received 500 µL FA working solution  
910 (400 µM) or vehicle (BSA+EtOH). Cells were treated at 200 µM for 48 hr. Treated cells were  
911 transferred to a deep 96 well plate and medium was discarded after centrifugation at 500 x g for  
912 5 min. Cells were washed once with 1000 µL D-PBS (Sigma). Next, cells were resuspended in  
913 300 µL binding buffer containing annexin-FITC and propidium iodide according to the  
914 manufacturer's protocol (BD Biosciences) and transferred to a shallow 96 well V-bottom plate  
915 (Corning). After staining for 15 min at room temperature in the dark, cells were washed once with  
916 300 µL binding buffer and finally resuspended in 100 µL binding buffer. Unstained and single stain  
917 controls were prepared for every cell line in a separate plate. Gates were adjusted such that 99%  
918 of unstained singlets fell below each threshold. See **Supplementary Figure 9** for complete gating  
919 strategy. Flow cytometry data were collected using a FACSCelesta analyzer equipped with an  
920 autosampler (BD Biosciences) and analyzed using FlowJo 10.5.3. Results shown are  
921 representative of three independent experiments conducted with sequential passages of each  
922 cell line.

923

924

925 **Metabolomics Analysis**

926

927 This section describes the methods used within **Figure 5d** and **Supplementary Figure 7**.

928 Metabolomics data acquired from Supplementary table 1 of Li *et al.*<sup>70</sup> For analysis, normalized

929 data ("1-clean data") and coefficient of variation for each metabolite ("1-CV") was used.

930 Normalized data was filtered to select only AML cells that were present in Avana 2020q4<sup>49</sup> screen

931 set. Following filtering, the median of species present were taken, grouped by whether the

932 measurement was from a FASTS AML or other AML cell line. The difference in median,

933 representing the log ratio, was taken for each metabolite. Metabolites that had differences in

934 medians less than the coefficient of variation were omitted from the plots. Acyl group and number

935 of unsaturated bonds were obtained directly from the provided nomenclature.

936

937 **AML Patient Survival Analysis**

938

939 This section describes the methods used within **Figure 6** and **Supplementary Figure 8 & 10**.

940 The results published here are in part based upon data generated by the Therapeutically

941 Applicable Research to Generate Effective Treatments (TARGET) initiative, phs000218,

942 managed by the NCI. The data used for this analysis are available at dbGaP Study Accession:

943 phs000465.v19.p8. Information about TARGET can be found at

944 <http://ocg.cancer.gov/programs/target>.

945

946 Genes chosen for analysis were all genes shown to have an interaction with ACACA in **Figure**

947 **4h** and FASN. Gene annotations noted in the **Figure 6a** heatmap include any non-silent mutation,

948 copy number loss for TP53 & KMT2A, and copy number gain for KRAS, NRAS, and FLT3. FLT3-

949 ITD annotations were included in the FLT3 annotation row bar. Mutation annotations come from

950 CCLE<sup>69</sup>, copy number calls come from the cBioPortal<sup>127,128</sup> database, and FLT-ITD annotations

951 come from the DSMZ catalogue<sup>129</sup>.

952

953 TARGET-AML<sup>71</sup> data including age, genetic expression (HTseq FPKM UQ) , time to event, and

954 survival event outcomes, and TCGA<sup>72</sup> patient ages and genetic expression were downloaded

955 directly from the Xena<sup>130</sup> database. The OHSU BeatAML<sup>73</sup> age data was directly downloaded

956 from the Vizome database, and genetic expression data was taken from the original publication.

957 Age of patient derived cell lines were obtained from the Cellosaurus database<sup>131</sup>. Hazard ratios  
958 calculated from Cox proportional hazards modeling were done using the R survival<sup>105,106</sup> package.  
959 Patient clustering stratification was done with clustering functions from the scipy package<sup>77</sup>, using  
960 Euclidean clustering and complete linkage settings. This output heatmap (**Figure 6e**) was created  
961 using functions from the seaborn<sup>109</sup> package. We identified the patient cluster containing the  
962 highest overall expression of CHP1, GPAT4, GPI, PCGF1 from the heatmap using the fcluster  
963 function from scipy<sup>77</sup>. **Figure 6f** demonstrates the resulting survival comparison of the two patient  
964 clusters and was created with functions from the lifelines<sup>111</sup> package, specifically,  
965 KaplanMeierFitter function for the Kaplan Meier curve, and the p-value reflecting the calculated  
966 logrank test of the two curves.

967  
968 P-values related to schoenfeld tests calculated internally by the survminer package. For TARGET  
969 data analysis, patient expression profiles were chosen from primary tumor samples, filtering out  
970 samples from recurrent patients (42 such cases). Patient stratification is conducted based on  
971 stratifying patient groups into lower genetic expression (patients with genetic expression below  
972 the 75th percentile, n = 108), and higher genetic expression (patients with 75th percentile and  
973 above, n = 37). Computed hazard ratios for all tested genes within the TARGET cohort all passed  
974 the cox proportion hazards assumption (**Supplementary Figure 10**) by failing to reject the  
975 schoenfeld test null hypothesis.

976  
977 **Supplementary Tables**

978  
979 **Table S1. Mixed Distribution Model Z-Score Matrix.** 808 cell line vs 18,111 gene matrix of  
980 mixed Z-score derived from log fold-change fitness scores.

981  
982 **Table S2. COSMIC TSG PS Statistics.** Statistics of 116 COSMIC TSG genes when observed  
983 as a PS, vs other available data points. Includes number of times TSG is observed as a PS  
984 gene (count), mean and median TPM expression when observed as a PS gene and additional  
985 backgrounds (PS\_Mean\_Exp, Other\_Mean\_Exp, PS\_Median\_Exp, Other\_Median\_Exp), and  
986 non-silent mutation rate as a PS gene and additional backgrounds (PS\_mut, Other\_mut).

987 Additionally includes a column of fisher's exact test comparing mutated vs non mutated  
988 observations, and a Wilcox test comparing expression levels for each gene.

989

990 **Table S3. PSG Co-PS network.** Network of PSG co-occurrence observations related to  
991 **Figures 2c and S4c**, including fisher test metrics (p-value and FDR).

992

993 **Table S4. enCas12a Screen Gene Selection and Rationale.**

994

995 **Table S5. enCas12a Library Design.**

996

997 **Table S6. enCas12a Single Gene Knock-Out Measurements.** Z-score of mean Log fold-  
998 change.

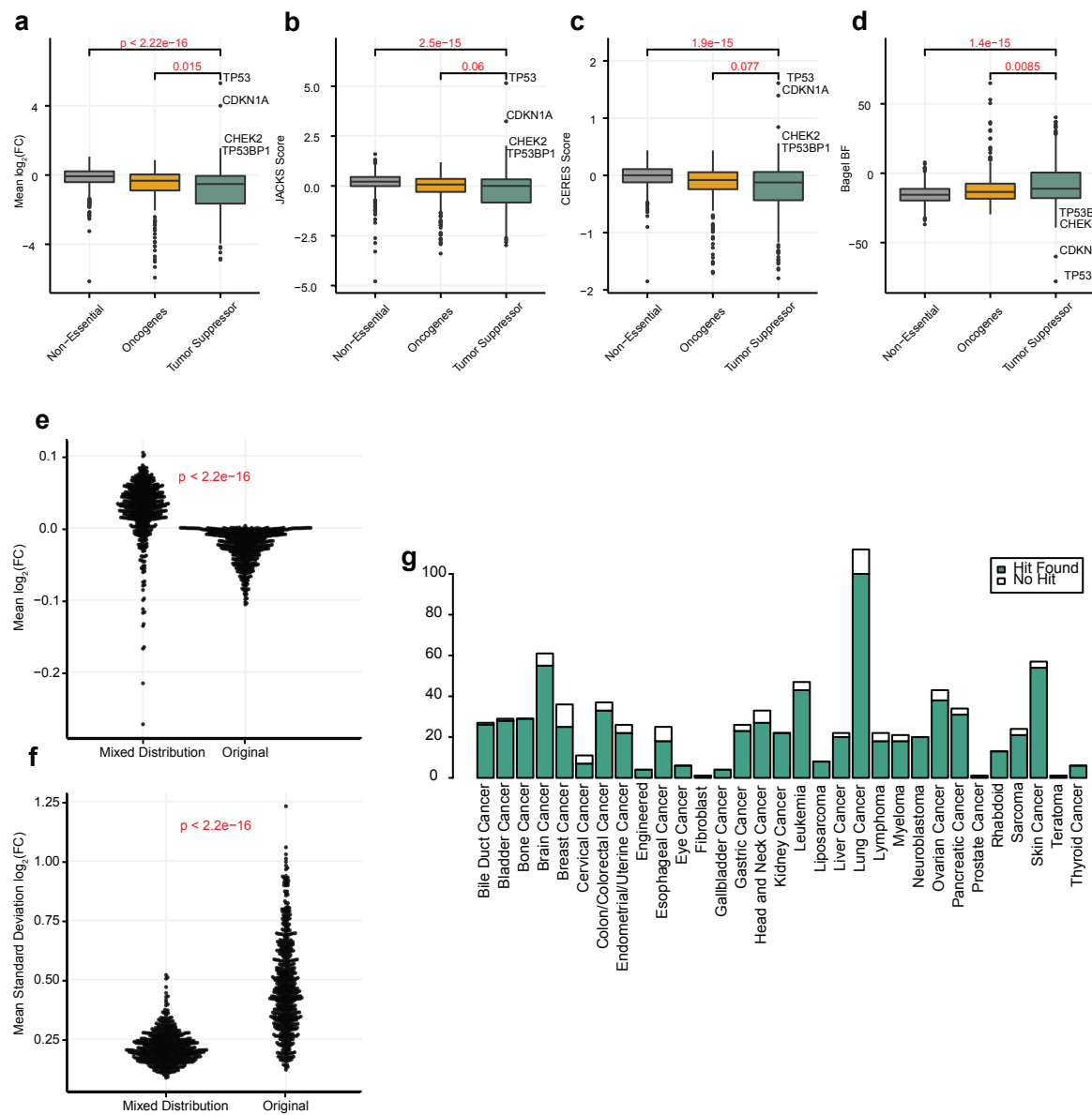
999

1000 **Table S7. enCas12a Double Gene Knock-Out Measurements.** Calculated Log fold-change  
1001 and corresponding GI Scores for each gene pair.

1002

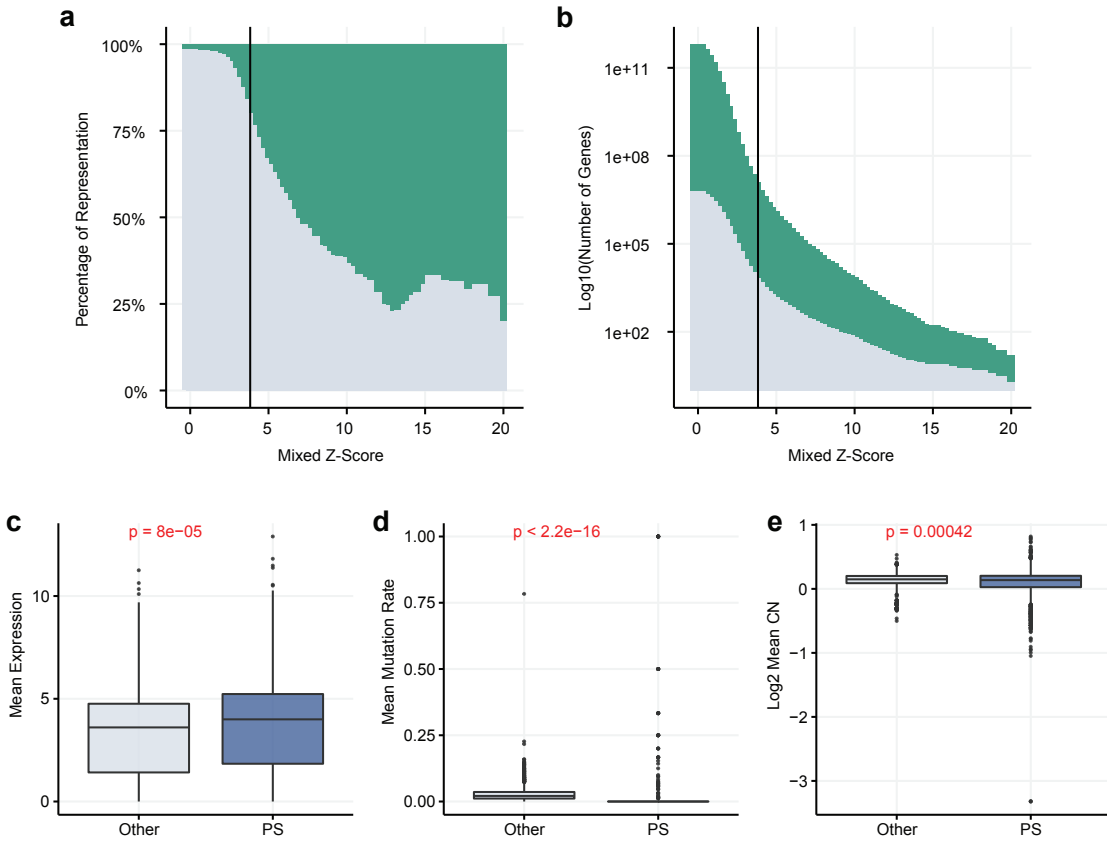
1003

1004 **Supplementary figure legends**



1005

1006  
1007  
1008 **Figure S1. Discovery of Proliferation Suppressor genes extended.** Fitness scoring  
1009 distributions of non-essential genes, and non-overlapping COSMIC defined oncogenes and tumor  
1010 suppressor genes; (a) mean log fold-change, (b) JACKS, (c) CERES, and (d) BAGEL. Selected  
1011 screen for a-d matches the screen observed in Figure 1a. (e) Distribution of mean log fold-change  
1012 of original distribution and mixed distribution . (f) Same (e) with mean standard deviation. (g) Bar  
1013 chart by cell line lineage, where at least 1 PS gene at 10% FDR cutoff identified.  
1014

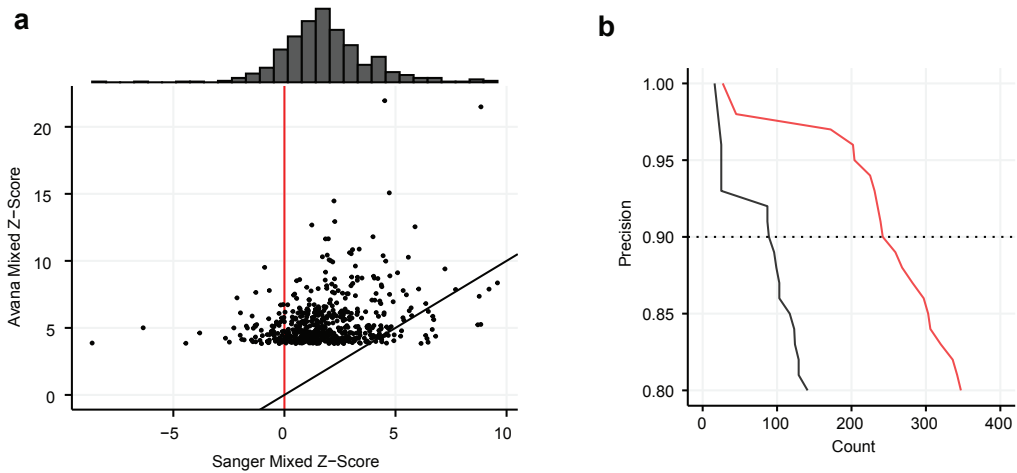


1015

1016

1017 **Figure S2. Proliferation Suppressor Gene Evidence.** (a) Percent representation of COSMIC  
1018 TSG (green) by corresponding label-shuffled Z-score. (b) Same as (a) with log10 y-axis of number  
1019 of genes. (c) Mean TPM expression of PSG, grouped by PS observations (blue) vs every other  
1020 available observation (gray) in which PSG were not observed as a PS. P value represents the  
1021 corresponding Wilcoxon test. (d) same as (c) with mutation rate and (e) copy number.  
1022

1023

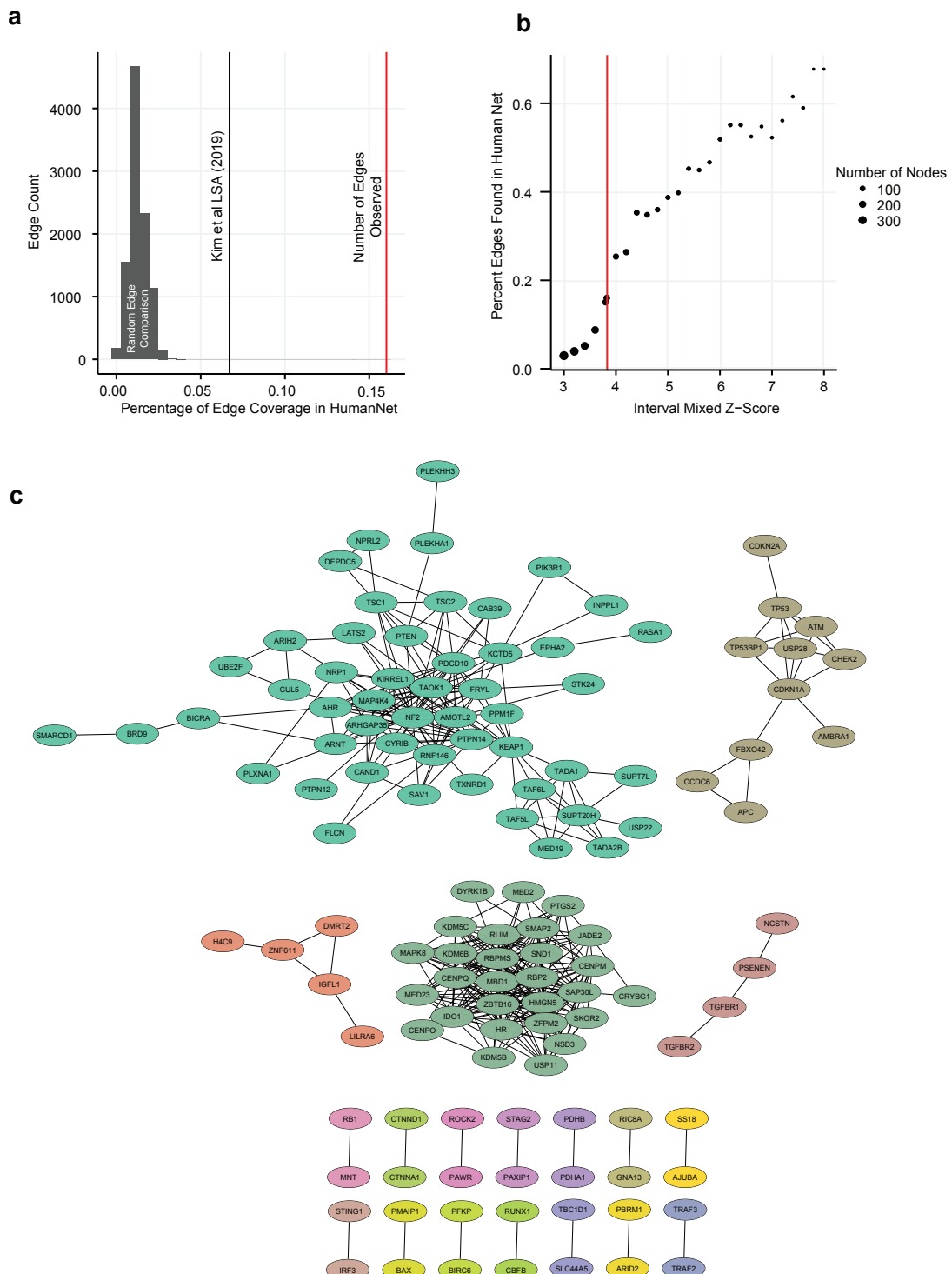


1024

1025

1026 **Figure S3. Avana vs Sanger Genetic Screens Comparison.** (a) Precision vs. recall of mixed  
1027 Z-score in matching screens from Avana (red), and Sanger (black). Dashed line, 90% precision  
1028 (10% FDR). (b) Avana vs Sanger mixed Z-scores of genes identified as hits in Avana.

1029



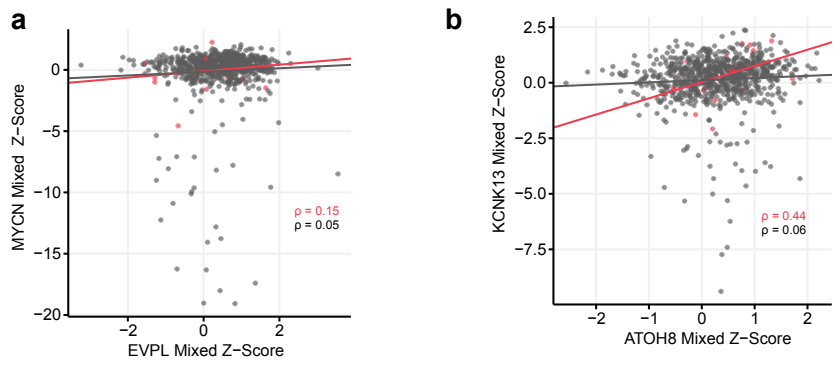
1030

1031

1032

1033 **Figure S4. Co-occurrence of PS genes extended.** (a) Empirical comparison of Co-PS network  
1034 edges. Distribution represents random edges between genes identified in the network, and the  
1035 percentage of edges identified in HumanNet with coessentiality network removed. Black line  
1036 represents the percent of edges identified in the Kim *et al.* coessentiality network. Red line  
1037 indicates the actual number of edges the Co-PS contains that are observed in HumanNet with  
1038 coessentiality network removed. (b) Percent of edge coverage observed in HumanNet with  
1039 coessentiality network removed against Co-PS edge FDR < 0.1%. networks at iterative label  
1040 shuffled Z-score cutoffs. Red dot indicates actual cutoff used. (c) Remaining modules from the  
1041 Co-PS network not included in Figure 2c.

1042



1044 **Figure S5. Examples of high dPCC resulting from data noise.** (a) EVPL vs MYCN mixed Z-  
1045 scores. Red indicates AML only observations, while gray indicates observations in all other cells.  
1046 (b) same as (a) for ATOH8 vs. KNCK13 mixed Z-scores.

1047

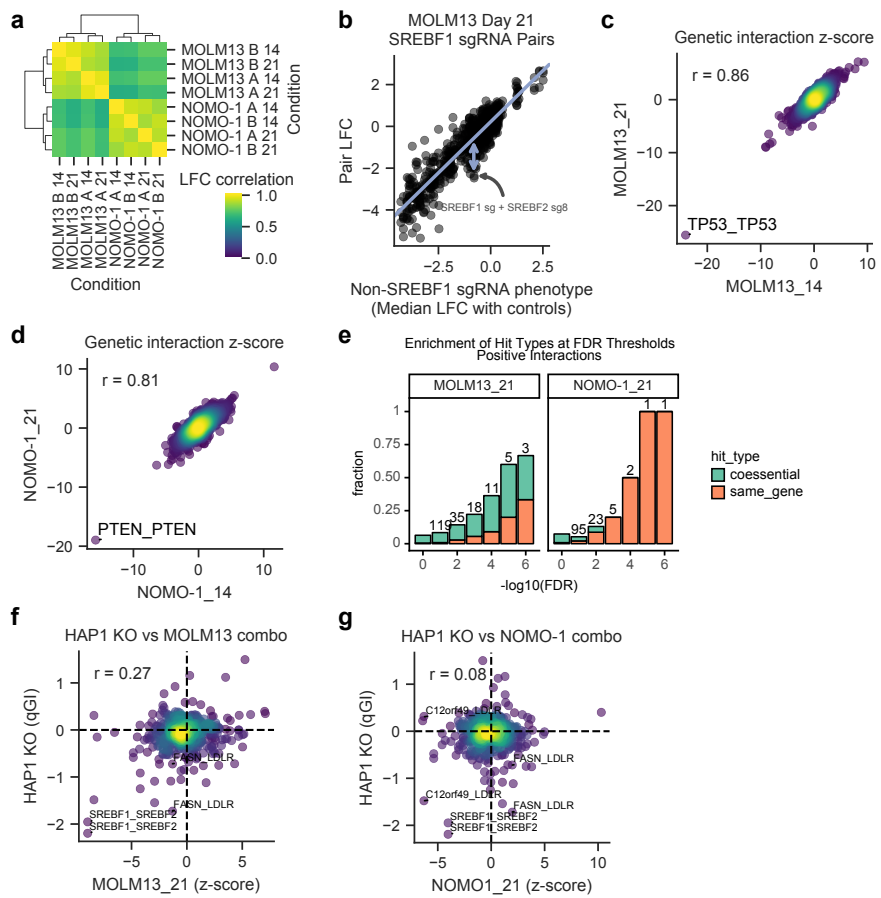


Figure S6

1048

1049

1050 **Figure S6. Combinatorial screen QC.** (a) Replicate correlations. (b) Example calculation of  
1051 residuals. (c) Correlation between genetic interaction scores for MOLM13. (d) same as (c) for  
1052 NOMO1. (e) Fraction of coessential pairs or pairs that target the same gene at different FDR  
1053 cutoffs for interactions with positive z-scores. (f) Comparison with qGI scores from Aregger *et al.*  
1054 for MOLM13. (g) Same as (f) for NOMO1.

1055

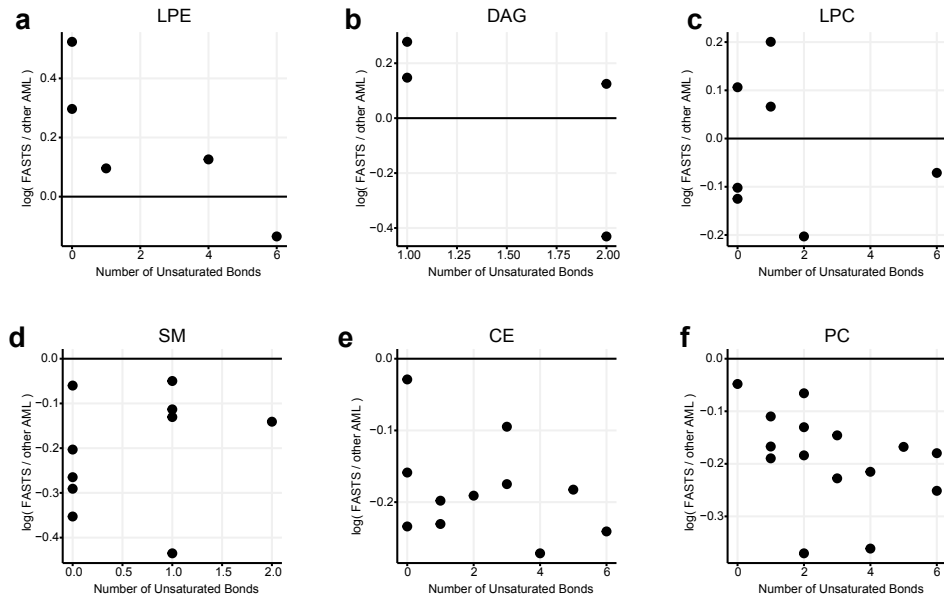


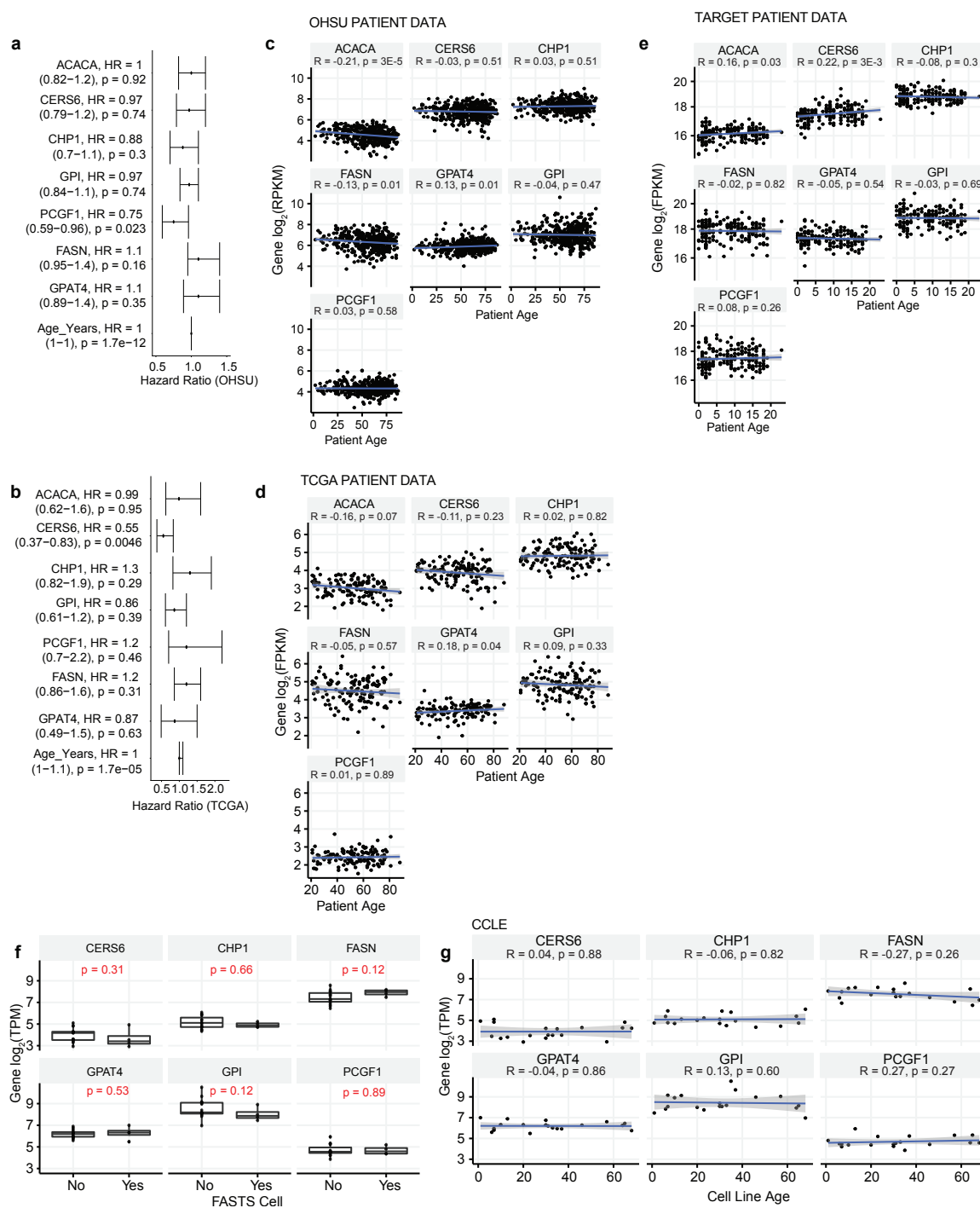
Figure S7

1056

1057

1058 **Figure S7. Additional metabolite comparisons.** (a) Lysophosphatidylethanolamine (LPE)  
1059 species metabolite difference. The x axis represents the median difference of log10 normalized  
1060 peak area of the metabolite in FASTS cells vs all other AML cells. The y axis represents the  
1061 number of saturated bonds present. Each dot represents a unique metabolite. (b) same for  
1062 diacylglycerol (DAG), (c) lysophosphatidylcholine (LPC), (d) sphingomyelin (SM), (e) cholesterol  
1063 ester (CE), and (f) phosphatidylcholine (PC) species.

1064



1067 **Figure S8. Comparisons of FAS genes against age in AML patient data.** Hazard ratio  
1068 calculations for FAS cluster genes in AML patient data coming from (a) OHSU - Tyner *et al.*, and  
1069 (b) TCGA LAML. Spearman correlations of patient age against FAS gene expression in (c) OHSU,  
1070 Tyner *et al.*, (d) TCGA LAML, and (e) GDC TARGET AML. (f) Boxplots of FAS gene expression  
1071 in FASTS AML cell lines and non-FASTS AML cell lines from CCLE. (g) Spearman correlations  
1072 of patient derived cell line age against FAS gene expression, coming from data in CCLE. ACACA  
1073 is not included in (g) as it was not found in the CCLE expression data used in prior analysis.  
1074

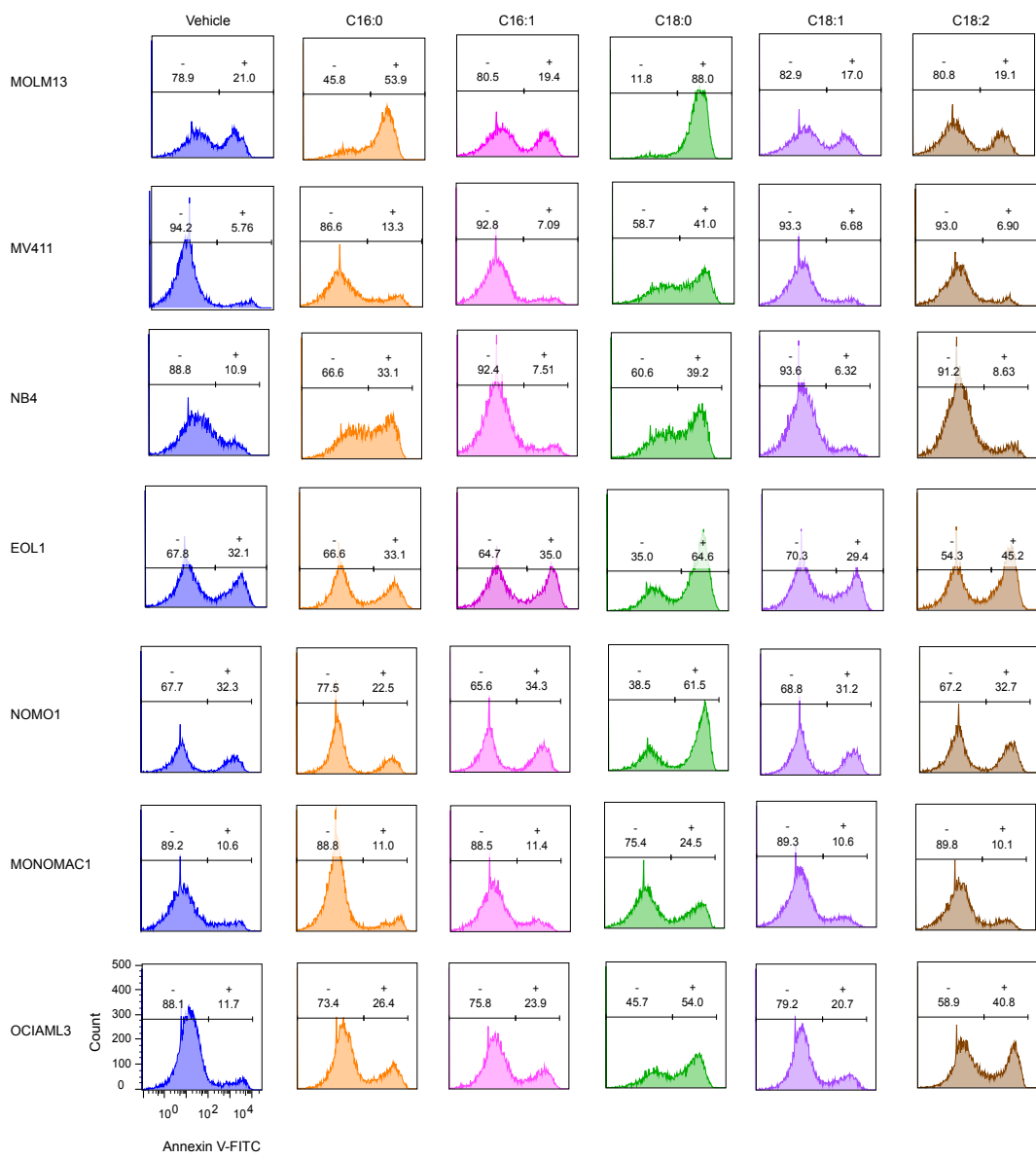
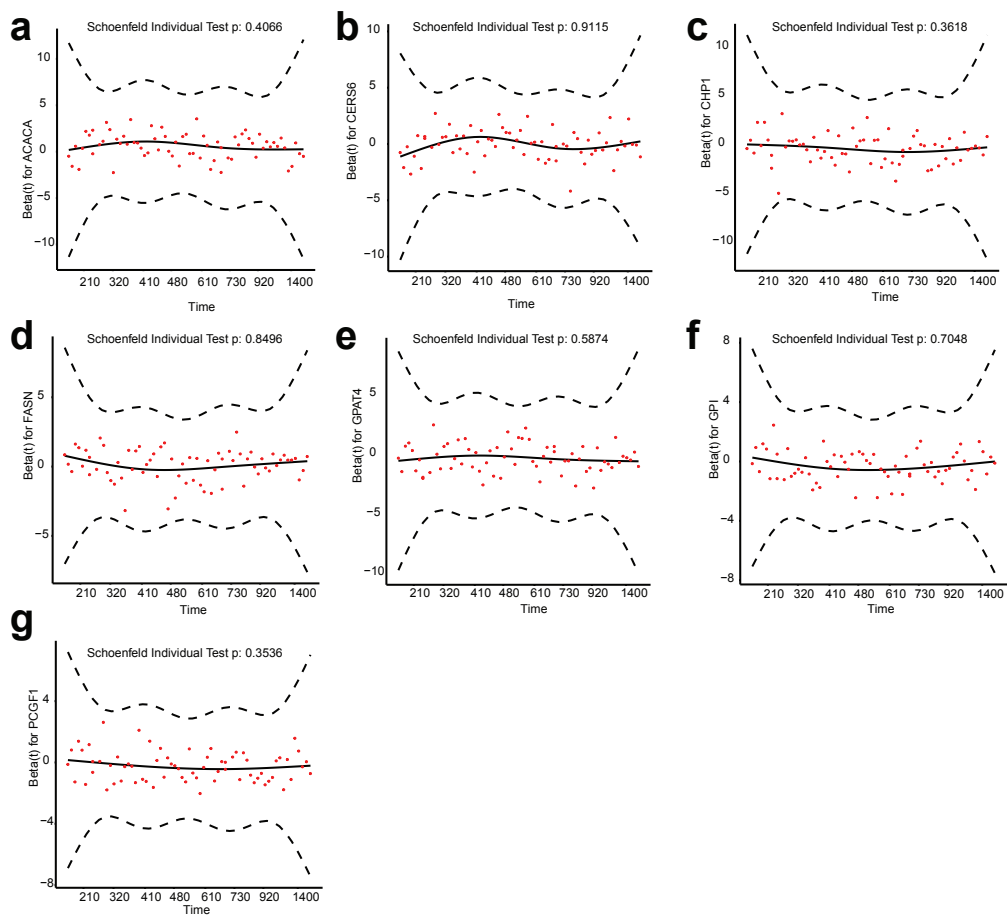


Figure S8

1075

1076

1077 **Figure S9. Sample flow cytometry plots.** A representative flow cytometry data used to create  
1078 bar graphs shown in figure 5b-c.  
1079



1080

1081

1082 **Figure S10. Testing the Cox Proportional Hazards Assumption.** Assessing the Cox  
1083 proportional hazards assumption with Schoenfeld tests of all genes in Figure 6d; (a) ACACA, (b)  
1084 CERS6, (c) CHP1, (d)FASN, (e) GPAT4, (f) GPI, (g) PCGF1.  
1085  
1086

1087 **References**

1088

1089 1. Jinek, M. *et al.* A Programmable Dual-RNA–Guided DNA Endonuclease in Adaptive Bacterial  
1090 Immunity. *Science* **337**, 816–821 (2012).

1091 2. Mali, P. *et al.* RNA-Guided Human Genome Engineering via Cas9. *Science* **339**, 823–826  
1092 (2013).

1093 3. Mali, P., Esvelt, K. M. & Church, G. M. Cas9 as a versatile tool for engineering biology.  
1094 *Nature Methods* **10**, 957–963 (2013).

1095 4. Cong, L. *et al.* Multiplex genome engineering using CRISPR/Cas systems. *Science (New  
1096 York, N.Y.)* **339**, 819–823 (2013).

1097 5. Shalem, O., Sanjana, N. E. & Zhang, F. High-throughput functional genomics using CRISPR-  
1098 Cas9. *Nat. Rev. Genet.* **16**, 299–311 (2015).

1099 6. Wang, T., Wei, J. J., Sabatini, D. M. & Lander, E. S. Genetic screens in human cells using  
1100 the CRISPR-Cas9 system. *Science* **343**, 80–84 (2014).

1101 7. Hart, T. *et al.* High-Resolution CRISPR Screens Reveal Fitness Genes and Genotype-  
1102 Specific Cancer Liabilities. *Cell* **163**, 1515–1526 (2015).

1103 8. Wang, T. *et al.* Identification and characterization of essential genes in the human genome.  
1104 *Science* **350**, 1096–1101 (2015).

1105 9. Aguirre, A. J. *et al.* Genomic Copy Number Dictates a Gene-Independent Cell Response to  
1106 CRISPR/Cas9 Targeting. *Cancer Discovery* **6**, 914–929 (2016).

1107 10. Meyers, R. M. *et al.* Computational correction of copy number effect improves specificity  
1108 of CRISPR-Cas9 essentiality screens in cancer cells. *Nat. Genet.* **49**, 1779–1784 (2017).

1109 11. Tsherniak, A. *et al.* Defining a Cancer Dependency Map. *Cell* **170**, 564–576.e16 (2017).

1110 12. Tzelepis, K. *et al.* A CRISPR Dropout Screen Identifies Genetic Vulnerabilities and  
1111 Therapeutic Targets in Acute Myeloid Leukemia. *Cell Rep* **17**, 1193–1205 (2016).

1112 13. Behan, F. M. *et al.* Prioritization of cancer therapeutic targets using CRISPR-Cas9  
1113 screens. *Nature* **568**, 511–516 (2019).

1114 14. Lagziel, S., Lee, W. D. & Shlomi, T. Inferring cancer dependencies on metabolic genes  
1115 from large-scale genetic screens. *BMC biology* **17**, 37 (2019).

1116 15. Rossiter, N. J. *et al.* CRISPR screens in physiologic medium reveal conditionally  
1117 essential genes in human cells. *Cell Metabolism* **33**, 1248-1263.e9 (2021).

1118 16. Zhao, D. *et al.* Combinatorial CRISPR-Cas9 Metabolic Screens Reveal Critical Redox  
1119 Control Points Dependent on the KEAP1-NRF2 Regulatory Axis. *Molecular Cell* **69**, 699–  
1120 708.e7 (2018).

1121 17. Aregger, M. *et al.* Systematic mapping of genetic interactions for de novo fatty acid  
1122 synthesis identifies C12orf49 as a regulator of lipid metabolism. *Nature Metabolism* **2**, 499–  
1123 513 (2020).

1124 18. Wang, T. *et al.* Gene Essentiality Profiling Reveals Gene Networks and Synthetic Lethal  
1125 Interactions with Oncogenic Ras. *Cell* **168**, 890-903.e15 (2017).

1126 19. Boyle, E. A., Pritchard, J. K. & Greenleaf, W. J. High-resolution mapping of cancer cell  
1127 networks using co-functional interactions. *Mol. Syst. Biol.* **14**, e8594 (2018).

1128 20. Rauscher, B. *et al.* Toward an integrated map of genetic interactions in cancer cells.  
1129 *Molecular Systems Biology* **14**, e7656 (2018).

1130 21. Kim, E. *et al.* A network of human functional gene interactions from knockout fitness  
1131 screens in cancer cells. *Life Science Alliance* **2**, (2019).

1132 22. Kegel, B. D. & Ryan, C. J. Paralog buffering contributes to the variable essentiality of  
1133 genes in cancer cell lines. *PLOS Genetics* **15**, e1008466 (2019).

1134 23. Dede, M., McLaughlin, M., Kim, E. & Hart, T. Multiplex enCas12a screens detect  
1135 functional buffering among paralogs otherwise masked in monogenic Cas9 knockout  
1136 screens. *Genome Biology* **21**, 262 (2020).

1137 24. Beltrao, P., Cagney, G. & Krogan, N. J. Quantitative genetic interactions reveal  
1138 biological modularity. *Cell* **141**, 739–745 (2010).

1139 25. Costanzo, M. *et al.* The genetic landscape of a cell. *Science* **327**, 425–431 (2010).

1140 26. Costanzo, M. *et al.* A global genetic interaction network maps a wiring diagram of  
1141 cellular function. *Science* **353**, (2016).

1142 27. Martin, H. *et al.* Differential genetic interactions of yeast stress response MAPK  
1143 pathways. *Molecular Systems Biology* **11**, 800 (2015).

1144 28. Wong, A. S. L. *et al.* Multiplexed barcoded CRISPR-Cas9 screening enabled by  
1145 CombiGEM. *PNAS* **113**, 2544–2549 (2016).

1146 29. Shen, J. P. *et al.* Combinatorial CRISPR–Cas9 screens for de novo mapping of genetic  
1147 interactions. *Nature Methods* **14**, 573–576 (2017).

1148 30. Han, K. *et al.* Synergistic drug combinations for cancer identified in a CRISPR screen for  
1149 pairwise genetic interactions. *Nature Biotechnology* **35**, 463–474 (2017).

1150 31. Najm, F. J. *et al.* Orthologous CRISPR-Cas9 enzymes for combinatorial genetic screens.  
1151 *Nature Biotechnology* **36**, 179–189 (2018).

1152 32. Du, D. *et al.* Genetic interaction mapping in mammalian cells using CRISPR  
1153 interference. *Nat Methods* **14**, 577–580 (2017).

1154 33. Horlbeck, M. A. *et al.* Mapping the Genetic Landscape of Human Cells. *Cell* **174**, 953–  
1155 967.e22 (2018).

1156 34. DeWeirdt, P. C. *et al.* Optimization of AsCas12a for combinatorial genetic screens in  
1157 human cells. *Nature Biotechnology* 1–11 (2020) doi:10.1038/s41587-020-0600-6.

1158 35. Kleinstiver, B. P. *et al.* Engineered CRISPR-Cas12a variants with increased activities  
1159 and improved targeting ranges for gene, epigenetic and base editing. *Nat. Biotechnol.* **37**,  
1160 276–282 (2019).

1161 36. Bandyopadhyay, S. *et al.* Rewiring of genetic networks in response to DNA damage.  
1162 *Science (New York, N.Y.)* **330**, 1385–1389 (2010).

1163 37. Ideker, T. & Krogan, N. J. Differential network biology. *Molecular Systems Biology* **8**, 565  
1164 (2012).

1165 38. Colic, M. *et al.* Identifying chemogenetic interactions from CRISPR screens with drugZ.  
1166 *Genome Med* **11**, 52 (2019).

1167 39. Menendez, J. A. & Lupu, R. Fatty acid synthase (FASN) as a therapeutic target in breast  
1168 cancer. *Expert Opin. Ther. Targets* **21**, 1001–1016 (2017).

1169 40. Search of: FASN - List Results - ClinicalTrials.gov.  
1170 <https://clinicaltrials.gov/search?cond=FASN> (2020).

1171 41. Hart, T. & Moffat, J. BAGEL: a computational framework for identifying essential genes  
1172 from pooled library screens. *BMC Bioinformatics* **17**, 164 (2016).

1173 42. Kim, E. & Hart, T. Improved analysis of CRISPR fitness screens and reduced off-target  
1174 effects with the BAGEL2 gene essentiality classifier. *Genome Medicine* **13**, 2 (2021).

1175 43. Allen, F. *et al.* JACKS: joint analysis of CRISPR/Cas9 knockout screens. *Genome Res.*  
1176 **29**, 464–471 (2019).

1177 44. Daley, T. P. *et al.* CRISPhieRmix: a hierarchical mixture model for CRISPR pooled  
1178 screens. *Genome Biol* **19**, 159 (2018).

1179 45. Bamford, S. *et al.* The COSMIC (Catalogue of Somatic Mutations in Cancer) database  
1180 and website. *Br J Cancer* **91**, 355–358 (2004).

1181 46. Sondka, Z. *et al.* The COSMIC Cancer Gene Census: describing genetic dysfunction  
1182 across all human cancers. *Nature Reviews Cancer* **18**, 696–705 (2018).

1183 47. Hart, T., Brown, K. R., Sircoulomb, F., Rottapel, R. & Moffat, J. Measuring error rates in  
1184 genomic perturbation screens: gold standards for human functional genomics. *Molecular  
1185 Systems Biology* **10**, 733 (2014).

1186 48. Dempster, J. M. *et al.* Extracting Biological Insights from the Project Achilles Genome-  
1187 Scale CRISPR Screens in Cancer Cell Lines. *bioRxiv* 720243 (2019) doi:10.1101/720243.

1188 49. DepMap 20Q4 Public. (2020) doi:10.6084/m9.figshare.13237076.v4.

1189 50. James, M. F. *et al.* NF2/merlin is a novel negative regulator of mTOR complex 1, and  
1190 activation of mTORC1 is associated with meningioma and schwannoma growth. *Mol. Cell. Biol.* **29**, 4250–4261 (2009).

1192 51. Huang, J., Dibble, C. C., Matsuzaki, M. & Manning, B. D. The TSC1-TSC2 complex is  
1193 required for proper activation of mTOR complex 2. *Mol. Cell. Biol.* **28**, 4104–4115 (2008).

1194 52. Marchi, S. *et al.* Defective autophagy is a key feature of cerebral cavernous  
1195 malformations. *EMBO Mol Med* **7**, 1403–1417 (2015).

1196 53. Zhu, Y. *et al.* Loss of endothelial programmed cell death 10 activates glioblastoma cells  
1197 and promotes tumor growth. *Neuro-oncology* **18**, 538–548 (2016).

1198 54. Pópulo, H., Lopes, J. M. & Soares, P. The mTOR signalling pathway in human cancer.  
1199 *Int J Mol Sci* **13**, 1886–1918 (2012).

1200 55. Massagué, J. G1 cell-cycle control and cancer. *Nature* **432**, 298–306 (2004).

1201 56. Evan, G. I. & Vousden, K. H. Proliferation, cell cycle and apoptosis in cancer. *Nature*  
1202 **411**, 342–348 (2001).

1203 57. Donehower, L. A. *et al.* Integrated Analysis of TP53 Gene and Pathway Alterations in  
1204 The Cancer Genome Atlas. *Cell Rep* **28**, 1370-1384.e5 (2019).

1205 58. Zhang, Y. *et al.* A Pan-Cancer Proteogenomic Atlas of PI3K/AKT/mTOR Pathway  
1206 Alterations. *Cancer Cell* **31**, 820-832.e3 (2017).

1207 59. Pan, J. *et al.* Interrogation of Mammalian Protein Complex Structure, Function, and  
1208 Membership Using Genome-Scale Fitness Screens. *Cell Syst* **6**, 555-568.e7 (2018).

1209 60. Bayraktar, E. C. *et al.* Metabolic coessentiality mapping identifies C12orf49 as a  
1210 regulator of SREBP processing and cholesterol metabolism. *Nat Metab* **2**, 487–498 (2020).

1211 61. Hwang, S. *et al.* HumanNet v2: human gene networks for disease research. *Nucleic  
1212 Acids Res* **47**, D573–D580 (2019).

1213 62. Khalid, A., Siddiqui, A. J., Huang, J.-H., Shamsi, T. & Musharraf, S. G. Alteration of  
1214 Serum Free Fatty Acids are Indicators for Progression of Pre-leukaemia Diseases to  
1215 Leukaemia. *Scientific Reports* **8**, 14883 (2018).

1216 63. Flavin, R., Peluso, S., Nguyen, P. L. & Loda, M. Fatty acid synthase as a potential  
1217 therapeutic target in cancer. *Future Oncology* **6**, 551–562 (2010).

1218 64. Punekar, S. & Cho, D. C. Novel Therapeutics Affecting Metabolic Pathways. *American  
1219 Society of Clinical Oncology Educational Book* e79–e87 (2019) doi:10.1200/EDBK\_238499.

1220 65. Roguev, A. *et al.* Conservation and rewiring of functional modules revealed by an  
1221 epistasis map in fission yeast. *Science* **322**, 405–410 (2008).

1222 66. Li, K.-C. Genome-wide coexpression dynamics: Theory and application. *Proc Natl Acad  
1223 Sci U S A* **99**, 16875–16880 (2002).

1224 67. Piccolis, M. *et al.* Probing the Global Cellular Responses to Lipotoxicity Caused by  
1225 Saturated Fatty Acids. *Molecular Cell* **74**, 32-44.e8 (2019).

1226 68. Zhu, X. G. *et al.* CHP1 Regulates Compartmentalized Glycerolipid Synthesis by  
1227 Activating GPAT4. *Mol. Cell* **74**, 45-58.e7 (2019).

1228 69. Ghandi, M. *et al.* Next-generation characterization of the Cancer Cell Line Encyclopedia.  
1229 *Nature* **569**, 503–508 (2019).

1230 70. Li, H. *et al.* The landscape of cancer cell line metabolism. *Nature Medicine* **25**, 850–860  
1231 (2019).

1232 71. Meshinchi, S. & Arceci, R. TARGET: Acute Myeloid Leukemia (AML), dbGaP Study  
1233 Accession: phs000465.v19.p8. [https://www.ncbi.nlm.nih.gov/projects/gap/cgi-bin/study.cgi?study\\_id=phs000465.v19.p8](https://www.ncbi.nlm.nih.gov/projects/gap/cgi-bin/study.cgi?study_id=phs000465.v19.p8) (2020).

1235 72. Genomic and Epigenomic Landscapes of Adult De Novo Acute Myeloid Leukemia. *New  
1236 England Journal of Medicine* **368**, 2059–2074 (2013).

1237 73. Tyner, J. W. *et al.* Functional genomic landscape of acute myeloid leukaemia. *Nature  
1238* **562**, 526–531 (2018).

1239 74. Gromelund, G. & Wickham, H. *R for Data Science*. (2020).

1240 75. The R Development Core Team. *R: A Language and Environment for Statistical*  
1241 *Computing*. (2016).

1242 76. Python Software Foundation. *Python Language Reference, version 3.8.2*. (2020).

1243 77. Virtanen, P. *et al.* SciPy 1.0: fundamental algorithms for scientific computing in Python.  
1244 *Nature Methods* **17**, 261–272 (2020).

1245 78. Harris, C. R. *et al.* Array programming with NumPy. *Nature* **585**, 357–362 (2020).

1246 79. Hunter, J. D. Matplotlib: A 2D Graphics Environment. *Computing in Science Engineering*  
1247 **9**, 90–95 (2007).

1248 80. McKinney, W. Data Structures for Statistical Computing in Python. *Proceedings of the*  
1249 *9th Python in Science Conference* 56–61 (2010) doi:10.25080/Majora-92bf1922-00a.

1250 81. Wickham, H. *et al.* Welcome to the Tidyverse. *Journal of Open Source Software* **4**, 1686  
1251 (2019).

1252 82. Dowle, M. *et al.* *data.table: Extension of ‘data.frame’*. (2020).

1253 83. Xie, Y. *et al.* *knitr: A General-Purpose Package for Dynamic Report Generation in R*.  
1254 (2020).

1255 84. Xie, Y. knitr: A Comprehensive Tool for Reproducible Research in R. *Implementing*  
1256 *Reproducible Research* 3–31 <https://www.taylorfrancis.com/> (2018)  
1257 doi:10.1201/9781315373461-1.

1258 85. Xie, Y. Dynamic Documents with R and knitr. *Routledge & CRC Press*  
1259 [https://www.routledge.com/Dynamic-Documents-with-R-and-knitr-2nd-](https://www.routledge.com/Dynamic-Documents-with-R-and-knitr-2nd-Edition/Xie/p/book/9781498716963)  
1260 *Edition/Xie/p/book/9781498716963* (2015).

1261 86. Benaglia, T., Chauveau, D., Hunter, D. & Young, D. mixtools: An R Package for  
1262 Analyzing Finite Mixture Models. *Journal of Statistical Software* **32**, (2009).

1263 87. Simpson, G. L., R Core Team, Bates, D. M. & Oksanen, J. *permute: Functions for*  
1264 *Generating Restricted Permutations of Data*. (2019).

1265 88. Keilwagen, J., Grosse, I. & Grau, J. Area under Precision-Recall Curves for Weighted  
1266 and Unweighted Data. *PLOS ONE* **9**, e92209 (2014).

1267 89. Grau, J., Grosse, I. & Keilwagen, J. PRROC: computing and visualizing precision-recall  
1268 and receiver operating characteristic curves in R. *Bioinformatics* **31**, 2595–2597 (2015).

1269 90. Durinck, S., Spellman, P. T., Birney, E. & Huber, W. Mapping identifiers for the  
1270 integration of genomic datasets with the R/Bioconductor package biomaRt. *Nat Protoc* **4**,  
1271 1184–1191 (2009).

1272 91. Durinck, S. *et al.* BioMart and Bioconductor: a powerful link between biological  
1273 databases and microarray data analysis. *Bioinformatics* **21**, 3439–3440 (2005).

1274 92. Carlson, M. org.Hs.eg.db. *Bioconductor* <http://bioconductor.org/packages/org.Hs.eg.db/>  
1275 (2018).

1276 93. Wilke, C. Streamlined Plot Theme and Plot Annotations for ‘ggplot2’.  
1277 <https://wilkelab.org/cowplot/> (2019).

1278 94. Clarke, E. & Sherrill-Mix, S. *ggbeeswarm: Categorical Scatter (Violin Point) Plots*.  
1279 (2017).

1280 95. Gentleman, R. *annotate: Annotation for microarrays*. (Bioconductor version: Release  
1281 (3.11), 2020). doi:10.18129/B9.bioc.annotate.

1282 96. Neuwirth, E. *RColorBrewer: ColorBrewer Palettes*. (2014).

1283 97. Gu, Z., Eils, R. & Schlesner, M. Complex heatmaps reveal patterns and correlations in  
1284 multidimensional genomic data. *Bioinformatics* **32**, 2847–2849 (2016).

1285 98. Warnes, G. R. *et al. gplots: Various R Programming Tools for Plotting Data*. (2020).

1286 99. Kassambara, A. ggplot2 Based Publication Ready Plots.  
1287 <https://rpkgs.datanovia.com/ggpubr/> (2020).

1288 100. Gu, Z., Gu, L., Eils, R., Schlesner, M. & Brors, B. circlize Implements and enhances  
1289 circular visualization in R. *Bioinformatics* **30**, 2811–2812 (2014).

1290 101. Arnold, J. B. *et al. ggthemes: Extra Themes, Scales and Geoms for ‘ggplot2’*. (2019).

1291 102. Attali, D. & Baker, C. *ggExtra: Add Marginal Histograms to 'ggplot2', and More 'ggplot2' Enhancements*. (2019).

1292 103. Pedersen, T. L. *patchwork: The Composer of Plots*. (2020).

1293 104. Wickham, H. *ggplot2: Elegant Graphics for Data Analysis*. (Springer, 2016).

1294 105. Therneau, T. M. & Grambsch, P. M. *Modeling Survival Data: Extending the Cox Model*. (Springer-Verlag, 2000). doi:10.1007/978-1-4757-3294-8.

1295 106. Therneau, T. M., until 2009), T. L. (original S->R port and R. maintainer, Elizabeth, A. & Cynthia, C. *survival: Survival Analysis*. (2020).

1296 107. Kassambara, A., Kosinski, M., Biecek, P. & Fabian, S. *survminer: Drawing Survival Curves using 'ggplot2'*. (2020).

1297 108. Python Software Foundation. *Python Language Reference, version 3.8.5*. (2020).

1298 109. Waskom, M. L. *seaborn: statistical data visualization*. *Journal of Open Source Software* **6**, 3021 (2021).

1299 110. Plotly Technologies Inc. *Collaborative data science*. (2015).

1300 111. Davidson-Pilon, C. *et al. CamDavidsonPilon/lifelines: 0.26.0*. (Zenodo, 2021). doi:10.5281/zenodo.4816284.

1301 112. Python Software Foundation. *Python Language Reference, version 3.8.3*. (2020).

1302 113. Pedersen, T. L. *tidygraph: A Tidy API for Graph Manipulation*. (2020).

1303 114. Pedersen, T. L. & RStudio. *ggraph: An Implementation of Grammar of Graphics for Graphs and Networks*. (2020).

1304 115. Seabold, S. & Perktold, J. *Statsmodels: Econometric and Statistical Modeling with Python*. 5 (2010).

1305 116. Hassan Kibirige *et al. has2k1/plotnine: v0.7.1*. (Zenodo, 2020). doi:10.5281/zenodo.3973626.

1306 117. DeWeirdt, P. C. *gnt: Python package for caidentifying Genetic iNTeractions from combinatorial screening data*. (2020).

1317 118. DeWeirdt, P. C. *gplot: Plotting functions for the Genetic Perturbation Platform's R&D*  
1318 *group at the Broad institute.* (2020).

1319 119. Pujar, S. *et al.* Consensus coding sequence (CCDS) database: a standardized set of  
1320 human and mouse protein-coding regions supported by expert curation. *Nucleic Acids Res.*  
1321 **46**, D221–D228 (2018).

1322 120. Iorio, F. *et al.* Unsupervised correction of gene-independent cell responses to CRISPR-  
1323 Cas9 targeting. *BMC Genomics* **19**, 604 (2018).

1324 121. Frankish, A. *et al.* GENCODE reference annotation for the human and mouse genomes.  
1325 *Nucleic Acids Res* **47**, D766–D773 (2019).

1326 122. Zerbino, D. R. *et al.* Ensembl 2018. *Nucleic Acids Res* **46**, D754–D761 (2018).

1327 123. Hart, T. *et al.* Evaluation and Design of Genome-Wide CRISPR/SpCas9 Knockout  
1328 Screens. *G3 (Bethesda)* **7**, 2719–2727 (2017).

1329 124. Shannon, P. *et al.* Cytoscape: A Software Environment for Integrated Models of  
1330 Biomolecular Interaction Networks. *Genome Res* **13**, 2498–2504 (2003).

1331 125. Luo, Y., Rana, P. & Will, Y. Palmitate increases the susceptibility of cells to drug-induced  
1332 toxicity: an in vitro method to identify drugs with potential contraindications in patients with  
1333 metabolic disease. *Toxicol. Sci.* **129**, 346–362 (2012).

1334 126. Alsabeeh, N., Chausse, B., Kakimoto, P. A., Kowaltowski, A. J. & Shirihi, O. Cell culture  
1335 models of fatty acid overload: Problems and solutions. *Biochim Biophys Acta Mol Cell Biol*  
1336 *Lipids* **1863**, 143–151 (2018).

1337 127. Gao, J. *et al.* Integrative analysis of complex cancer genomics and clinical profiles using  
1338 the cBioPortal. *Sci Signal* **6**, pl1 (2013).

1339 128. Cerami, E. *et al.* The cBio Cancer Genomics Portal: An Open Platform for Exploring  
1340 Multidimensional Cancer Genomics Data. *Cancer Discov* **2**, 401–404 (2012).

1341 129. German Collection of Microorganisms and Cell Cultures GmbH: Welcome to the Leibniz  
1342 Institute DSMZ. <https://www.dsmz.de/> (2020).

1343 130. Goldman, M. J. *et al.* Visualizing and interpreting cancer genomics data via the Xena  
1344 platform. *Nature Biotechnology* **38**, 675–678 (2020).

1345 131. Bairoch, A. The Cellosaurus, a Cell-Line Knowledge Resource. *J Biomol Tech* **29**, 25–38  
1346 (2018).

1347

1348

1349